buildings

MDPI

Article

Structural Performance and Boundary Effects of Dry-Jointed Sliding Masonry Infill Walls with Openings Under Sequential In-Plane and Out-of-Plane Loading

Ibrahim Serkan Misir [1,*], Ali Cihan Demir [2], Sadik Can Girgin [1], Okan Onal [1] and Cagrı Cetik [1]

[1] Civil Engineering Department, Dokuz Eylul University, Izmir 35390, Türkiye; sadik.girgin@deu.edu.tr (S.C.G.); okan.onal@deu.edu.tr (O.O.); cagri.cetik@deu.edu.tr (C.C.)
[2] Graduate School of Natural and Applied Sciences, Dokuz Eylul University, Izmir 35390, Türkiye; alicihan.demir@deu.edu.tr
* Correspondence: serkan.misir@deu.edu.tr

Abstract

Conventional masonry infill walls can significantly alter the seismic response of framed buildings and often produce damage patterns incompatible with resilience-based seismic design. Dry-jointed sliding masonry wall systems have therefore emerged as deformation-tolerant alternatives that accommodate drift through controlled interface motion rather than damage accumulation. This study investigates the sequential in-plane (IP) and out-of-plane (OOP) behavior of such systems considering wall thickness, openings, and boundary detailing. Six full-scale specimens were tested, including thick- and thin-wall reference specimens, thick-wall specimens with window openings, and thin-wall specimens with door openings. IP performance was evaluated using global hysteretic and energy-based response parameters, whereas OOP behavior was assessed through load–displacement response, an equivalent acceleration index, and selected image-based displacement fields. The results show that IP drift was mainly accommodated through distributed sliding along horizontal interfaces and local block rotation, without diagonal compression strut formation or brittle cracking, even at drift ratios up to approximately 3.5%. Wall thickness improved IP strength, stiffness, shear resistance, and cumulative energy dissipation, while openings mainly affected deformation compatibility and load-transfer continuity. Under OOP loading, wall thickness and boundary continuity increased stiffness and capacity while enabling resistance mobilization at smaller displacement levels. As inertia-based comparison indicators, boundary-enhanced thick- and thin-wall specimens reached equivalent acceleration capacities of 3.41 g and 1.64 g, respectively. Overall, the system reduced IP damage accumulation, but adequate OOP stability requires appropriate wall thickness, unit geometry, and boundary detailing.

Keywords: dry-jointed masonry; sliding infill wall; locked brick; in-plane response; out-of-plane stability; IP-OOP interaction; boundary detailing; image-based displacement measurement

Check for updates

Academic Editor: Marco Corradi

Received: 31 May 2026
Revised: 22 June 2026
Accepted: 24 June 2026
Published: 28 June 2026

Copyright: © 2026 by the authors. Licensee MDPI, Basel, Switzerland. This article is an open access article distributed under the terms and conditions of the Creative Commons Attribution (CC BY) license.

1. Introduction

Reinforced concrete (RC) frame buildings with masonry infill walls represent one of the most prevalent structural systems in seismic regions worldwide. Although infill panels are commonly classified as non-structural elements in design codes, extensive experimental and analytical research has demonstrated that their interaction with surrounding RC

frames substantially modifies global stiffness, strength, deformation demand, and failure mechanisms [1–5]. Therefore, the assumption that infills are structurally insignificant has repeatedly proven inconsistent with observed earthquake performance.

Post-earthquake reconnaissance reports from major seismic events, including the 1995 Kobe, 1999 Kocaeli, 2009 L'Aquila, 2011 Van, 2015 Gorkha, 2020 İzmir, and 2023 Kahramanmaraş earthquake sequence, have repeatedly highlighted the complex role of infill walls in both structural response and damage propagation in RC frame buildings [6–11]. Infilled RC frames frequently exhibit soft-story formation, torsional response due to asymmetric infill distribution, short-column effects, and premature out-of-plane (OOP) collapse of damaged panels. Such failures may cause life safety hazards and significant economic losses, particularly considering that non-structural components and building contents may account for more than 80% of total building value [12,13].

Conventional masonry infills typically resist in-plane (IP) lateral loading through a diagonal compression strut mechanism, which increases initial stiffness and strength but also causes localized cracking, brittle damage, and strong force transfer to the surrounding frame [14–16]. The brittle nature of masonry and the strong interaction between frame and infill may also trigger premature column shear failures [17]. Moreover, prior IP damage can significantly reduce subsequent OOP stability by modifying boundary conditions, degrading arching action, and weakening the wall panel. Experimental studies have shown that prior IP damage can reduce OOP capacity by up to 50% [18], and subsequent investigations have further confirmed the strong dependence of OOP resistance on IP-induced damage and boundary degradation [19–26].

Openings further complicate the seismic behavior of infilled frames. They reduce stiffness and load capacity, interrupt load-transfer paths, and alter deformation compatibility between wall segments [27–29]. Their influence becomes particularly important in engineered infill systems, where wall thickness, opening configuration, and boundary detailing may jointly control both IP deformation capacity and OOP stability.

These limitations have motivated the development of alternative infill systems that seek to reduce detrimental frame–infill interaction while maintaining stability. Among these, sliding and deformable infill systems are especially promising because they aim to replace brittle diagonal compression behavior with controlled kinematic deformation. The locked-brick infill concept introduced by Misir et al. (2012) [30] and further developed by Misir (2015) [31] represents one of the early attempts to promote distributed bed-joint slip while maintaining OOP stability through mechanical interlocking. However, although previous studies demonstrated improved drift capacity and deformation tolerance, the combined IP and OOP performance of such systems with openings and refined boundary details remains insufficiently quantified.

Despite the growing body of literature on engineered infill systems, several research gaps remain. First, the OOP stability of sliding or locked-brick infill walls after significant IP deformation has not been systematically quantified. Second, the combined influence of wall thickness, opening configuration, and boundary detailing on IP and OOP behavior of sliding wall systems remains unclear. Third, the role of refined boundary continuity in controlling OOP stiffness, load capacity, and deformation symmetry in sliding walls with openings requires further experimental clarification. Finally, coupled IP–OOP kinematics in discontinuous sliding infills require spatially resolved experimental evidence.

The present study addresses these gaps through full-scale experiments on six dry-jointed sliding masonry wall specimens. Four specimens incorporate centrally located openings: two thick-wall specimens with window openings and two thin-wall specimens with door openings. Two additional specimens without openings are included as reference configurations. The study evaluates IP cyclic response, strength and stiffness degradation,

energy dissipation, OOP load-carrying capacity, equivalent acceleration capacity, and selected image-based IP and OOP deformation fields. Particular emphasis is placed on the role of wall thickness, opening configuration, and boundary detailing in governing deformation compatibility, load transfer, and OOP stability.

2. Previous Works

2.1. Conventional Infill Response and IP–OOP Interaction

The seismic response of conventional masonry infills is commonly interpreted through their interaction with the surrounding RC frame. Under lateral loading, the infill panel engages with the frame and develops a diagonal compression mechanism, which increases initial stiffness and lateral strength but also produces localized stress transfer and damage concentration. Depending on masonry properties, frame stiffness, interface conditions, and loading history, the observed failure modes may include sliding shear, diagonal cracking, diagonal compression, corner crushing, and frame-dominated mechanisms [14,16]. Although these mechanisms can enhance initial resistance, they often reduce deformation capacity and may intensify damage in adjacent RC members, including premature column shear failures [17].

The vulnerability of infill panels becomes more critical when IP and OOP actions are considered sequentially. Prior IP cracking can degrade OOP resistance by altering contact conditions, weakening arching action, and reducing the effectiveness of boundary restraints. Early experimental studies demonstrated the sensitivity of OOP capacity to prior IP damage and provided further quantification of OOP strength in unreinforced masonry infill panels [18,19]. Subsequent studies confirmed the strong dependence of OOP capacity on IP-induced damage and boundary degradation [20–23]. More recent investigations by Demirel et al. (2023), Halici et al. (2023), and Zhang et al. (2023) [24–26] further emphasized the relevance of sequential IP–OOP interaction in assessing the residual stability of masonry infill walls. These studies collectively demonstrate that OOP stability cannot be assessed independently from the preceding IP deformation state in conventional infill walls.

Openings further modify the internal force-transfer mechanism of masonry infills. Experimental studies have shown that openings reduce stiffness and lateral strength, modify stress trajectories, and alter failure mechanisms depending on their size, position, and boundary treatment [27–29]. In conventional infill walls, openings may also promote damage localization, segmental response, and nonuniform boundary demands under combined IP and OOP loading.

2.2. Engineered, Sliding, and Decoupled Infill Systems

To overcome the limitations of conventional masonry infills, several enhancement and interaction-reduction strategies have been developed. Strengthening techniques such as fiber-reinforced polymer (FRP) overlays, textile-reinforced mortars (TRM), and bed-joint reinforcement improve shear and flexural capacity, but may also increase frame–infill interaction by enhancing panel stiffness and strength [32–34]. In contrast, interaction-reduction strategies aim to decouple the wall from the surrounding frame through intentional gaps, deformable joints, or flexible connectors [35–40].

Sliding and deformable infill systems represent a mechanism-oriented form of interaction reduction. Rather than relying on increased panel strength, they seek to reduce diagonal compression action and brittle cracking by allowing controlled joint slip, localized rotation, rocking, or distributed deformation. Such systems include frictional sliding fuses [41], locked-brick infills [30,42], sliding infills with horizontal joints [43], semi-interlocking masonry [44], unbonded brickwork [45], and vertically sliding infills [46]. These approaches aim to enhance post-earthquake damage control by accommodating

inter-story drift through controlled sliding and rotation instead of premature crushing or uncontrolled diagonal cracking [31,47–51].

Misir et al. (2012) [30] introduced the locked-brick infill concept to promote distributed bed-joint slip while maintaining OOP stability through mechanical interlocking features. Large-scale experiments demonstrated improved drift capacity and deformation tolerance relative to conventional masonry panels. Similar sliding-joint solutions based on subpanels were experimentally validated by Preti et al. (2012) [43] and numerically investigated by Bolis et al. (2017) [52], showing that intentionally introduced sliding interfaces can reduce the dominance of diagonal strut action and shift the response toward a more ductile, mechanism-based deformation mode.

Other systems have pursued the same objective through unbonded joints, rail-type connections, semi-interlocking units, vertically sliding configurations, or frictional devices. Palios et al. (2017) [45] introduced an unbonded brick infill system with mortar-free bed joints and rail-in-groove connections, enabling controlled sliding while maintaining OOP stability. Mohammadi et al. (2011) [41] proposed frictional sliding fuses to enhance ductility by concentrating energy dissipation along sliding interfaces. Semi-interlocking masonry systems and vertically sliding infills similarly rely on controlled relative movement while preserving wall stability [44,46].

More recent experimental campaigns have further clarified the importance of sequential IP–OOP interaction in both conventional and engineered infill systems [49,50,53–57]. Dynamic shaking-table tests on weak clay masonry infills with and without prior IP loading demonstrated that previous IP damage can substantially reduce OOP acceleration capacity and stability, particularly when boundary adherence and arching mechanisms are degraded [56]. Similarly, quasi-static IP/OOP tests on masonry-infilled RC frames with openings showed that previous IP damage weakened block bonding and wall–frame interface restraint, leading to reduced subsequent OOP load-bearing capacity [53]. Frame-isolated infills have also been shown to delay infill–frame interaction, reduce wall damage, and improve ductility under IP loading; however, their OOP response remains strongly dependent on boundary conditions, and flexible interfaces may reduce OOP strength unless sufficient side restraint is provided [50]. By contrast, innovative sliding-joint infills subjected to prior IP cyclic loading up to large drift levels exhibited limited damage and no collapse under demanding OOP shaking-table motions, indicating that properly detailed sliding mechanisms may reduce the detrimental coupling between IP damage and OOP stability [49]. Polyurethane-based flexible joints and fibre-grid protection systems have also been shown to delay infill damage, improve deformation compatibility, and protect infills against OOP collapse under severe dynamic demands [57]. Full-scale tests on RC frames with conventional and decoupled masonry infills have further shown that openings may promote damage localization and segmental response in conventional infills, whereas elastomeric interface elements can delay infill activation and reduce direct frame–wall interaction [54]. Nevertheless, even in specimens incorporating relatively thick elastomeric interface layers at the column and beam boundaries, compression-strut-related diagonal cracking was observed from about 1.8% IP drift, followed by corner crushing at larger drift levels [54]. These findings indicate that the effectiveness of decoupling depends strongly on boundary-detail continuity, material durability, and the ability of the system to avoid unintended reactivation at large drift levels or under combined IP–OOP loading. In addition, possible settlement effects associated with relatively thick elastomeric interface layers, the limited verification of thin-wall configurations with door openings under sequential IP and OOP loading, and the practical need for engineered infill systems constructed using conventional materials and techniques remain important issues for further investigation.

Therefore, recent evidence indicates that engineered infill systems should not be assessed only in terms of IP drift capacity, but also in terms of residual OOP stability, opening-induced segmentation, and boundary-detail compatibility. Addressing these multiple and interacting performance requirements has motivated the development of increasingly advanced analytical, numerical, and data-driven assessment approaches for masonry-infilled frame systems. Recent numerical and data-driven studies have also advanced the seismic assessment of infilled frame systems. Macro-models, refined finite-element approaches, database-based design formulations, and machine-learning tools have been increasingly used to estimate the contribution of masonry infills to global seismic response, residual drift, fragility, and OOP capacity [58]. Recent database-oriented studies have compiled experimental results for OOP and sequential IP–OOP infill response and have evaluated the predictive performance of available capacity models, while machine-learning-based tools have been proposed for seismic response assessment of structural frames considering masonry infills and soil–foundation–structure interaction [59]. These developments are important for building-level seismic assessment; however, their direct application to dry-jointed sliding infills remains challenging because the governing response involves discontinuous contact, interface sliding, block rotation, local restraint activation, and opening-induced segment interaction rather than a conventional diagonal-strut mechanism. The present experimental study therefore provides component-level evidence for dry-jointed sliding infills with different wall thicknesses and opening configurations, addressing a gap between recent IP–OOP assessment studies and low-damage engineered infill systems constructed without proprietary elastomeric or adhesive components.

2.3. Full-Field Measurement Techniques for Discontinuous Infill Mechanisms

The interpretation of sliding and discontinuous infill mechanisms requires spatially resolved displacement data. Conventional instruments, such as LVDTs and string potentiometers, provide accurate point measurements, but cannot fully capture block-wise motion, joint slip, local rotations, or deformation redistribution around openings. This limitation is critical for dry-jointed or sliding infill systems, where the response is governed by relative unit motion rather than continuous strain development. Contact-based sensors may also become vulnerable during large deformation stages, when information on local instability or residual OOP resistance is most needed [60,61].

Non-contact optical techniques provide an effective alternative for distributed deformation measurement. Digital Image Correlation (DIC) has been widely used in masonry and infilled-frame experiments to interpret crack initiation, deformation localization, and damage evolution [60,62,63]. However, DIC may be challenging in large-scale tests involving significant OOP displacement, surface discontinuity, joint opening, or block-wise sliding, since it generally requires a continuous high-contrast speckle pattern and sufficient image correlation [63].

Marker-based Structure-from-Motion (SfM) photogrammetry provides a complementary approach by reconstructing three-dimensional geometry from multi-view images and enabling non-contact 3D displacement tracking over large surfaces [64,65]. Recent studies showed that close-range or marker-based SfM can achieve sub-millimeter to millimeter-level precision under controlled laboratory conditions [66,67]. Unlike speckle-dependent DIC, marker-based SfM tracks discrete targets, making it suitable for monitoring masonry units or subpanels as rigid or semi-rigid bodies and identifying interface activation, localized sliding, rotation centers, and deformation redistribution around openings.

In engineered sliding infill walls, image-based full-field measurements can therefore complement conventional sensors by linking global force–displacement response to local

kinematic mechanisms, helping distinguish cracking-, arching-, and sliding-dominated responses and assess the effectiveness of boundary detailing in preserving OOP stability.

3. Experimental Program

3.1. Experimental Scope and Research Variables

This study investigates the seismic behavior of dry-jointed sliding masonry infill wall systems with openings under sequential in-plane (IP) and out-of-plane (OOP) loading (Figure 1). The experimental program was part of a broader research campaign comprising 21 tests on 13 full-scale specimens, with variations in wall geometry, unit configuration, opening type, and boundary detailing.

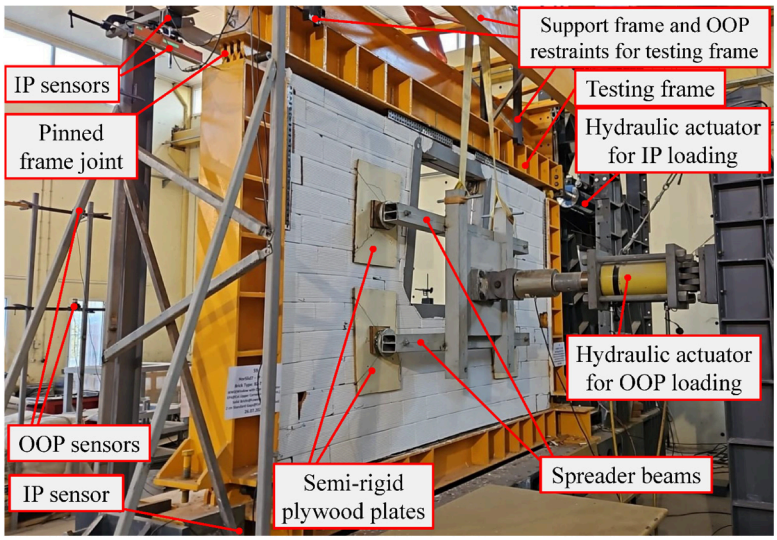

Figure 1. General view of bidirectional test setup.

Within this framework, the present study focuses primarily on four specimens with centrally located openings: TW1 and TW2, representing thick-wall specimens with window openings, and ND1 and ND2, representing thin-wall specimens with door openings. For reference, two additional specimens without openings are also considered: TR, representing the thick reference wall, and NR, representing the thin reference wall.

The selected specimens enable a controlled evaluation of the effects of wall thickness, opening configuration, and boundary continuity on both IP and OOP behavior. Particular emphasis is placed on the evolution of lateral load capacity, stiffness degradation, energy dissipation, and deformation mechanisms during IP loading.

The study further examines the post-IP OOP stability and load-carrying capacity of the specimens. OOP behavior is evaluated in terms of load–displacement response, deformation compatibility, and equivalent acceleration capacity with respect to inertia-induced seismic demands.

Marker-based image acquisition and photogrammetric processing techniques were also employed in selected tests to support the interpretation of global and local deformation mechanisms. Although full-field measurements were not available for all specimens and loading stages, the image-based results provide complementary insight into sliding patterns, deformation distribution, and kinematic compatibility within the wall systems.

3.2. Preliminary Experimental Development Tests

Prior to the final specimen series, four preliminary full-scale development tests (P1–P4) were conducted within the same research project. These specimens were not informal trials; rather, they were used to refine the sliding-wall concept, boundary details, and construction

sequence adopted in the final test series. The detailed load–displacement results of P1–P4 are not reported herein, since the present paper focuses on the six final specimens with and without openings. Nevertheless, these tests provided an experimental basis for selecting horizontal sliding interfaces, defining side-gap and EPS-strip arrangements, adjusting the extent of top-gap filler materials, and locating the OOP restraint elements.

The preliminary specimens did not contain door or window openings. Specimens P1–P3 were tested under IP loading only, whereas P4 was subjected to sequential IP and OOP loading. The investigations focused on the effectiveness of horizontal and vertical sliding interfaces, seismic gap dimensions, top-gap filler detailing, and OOP restraint arrangement.

In P1 and P2, thick interlocking clay units were arranged to promote either vertical or horizontal sliding mechanisms. Based on construction practicality and observed deformation characteristics, horizontal sliding interfaces provided more stable and predictable behavior and were therefore adopted in the subsequent specimens. P3 and P4 employed thicker and flatter interlocking units with more sliding interfaces and more tolerant interlocking geometries, which improved interface activation and sliding efficiency.

The preliminary tests also contributed to boundary-detail development. In P1–P3, 20 mm-wide seismic gaps were provided along both vertical wall boundaries and filled with compressible expanded polystyrene (EPS) strips, whereas P4 employed significantly smaller gaps without EPS filling. The observations indicated that larger compressible boundary gaps reduced undesirable frame–wall interaction and allowed the wall to accommodate larger drift demands without geometric locking. These findings led to the adoption of continuous EPS-filled seismic gaps in the final specimen configurations.

The top-gap detailing was also progressively refined. Polyurethane foam was initially applied along the top interface primarily to provide deformable OOP restraint, while limiting excessive vertical stress transfer was considered a secondary function. Based on compression concentrations observed near the wall toes under large drift demands, the foam-filled region was progressively narrowed toward the mid-span of the top beam in subsequent specimens, leaving larger unfilled zones near the beam ends. The foam was not applied in the TW-series specimens and was also omitted in ND2, where OOP stability was provided through extended steel restraint detailing. These observations indicated that minimizing vertical restraint, especially near wall ends, reduced localized toe crushing and improved deformation compatibility.

Finally, the OOP test on P4 confirmed that the interlocking geometry of the dry-jointed units could mobilize stable OOP resistance despite the absence of mortar. The test also highlighted the importance of providing OOP restraint near the column–beam joint regions, which subsequently influenced the arrangement of the steel restraint elements adopted in the final specimen configurations.

3.3. Interface Materials and Seismic Gaps

To reduce unintended frame–wall interaction and to provide controlled interface conditions, three auxiliary interface materials were incorporated into the specimen construction. A 3 mm-thick polymer-modified bituminous membrane strip, Osmanlı PP3 (Osmanlı İzolasyon, Izmir, Türkiye) was placed between the bottom brick course and the supporting steel beam in all specimens. The membrane was laid as a dry interfacial strip without heat welding or torch-applied bonding. According to the manufacturer's data, the material remains flexible within a temperature range of approximately -10 °C to 120 °C. Its areal weight and polyester reinforcement weight are approximately 33 N/m^2 and 1.6 N/m^2, respectively, while its tensile strength is about 4 MPa and its ultimate elongation in both lon-

gitudinal and transverse directions is approximately 30%. These material characteristics are specified according to TS 11758-1 [68] for polymer bituminous waterproofing membranes.

In this study, the bituminous membrane was not used for waterproofing, but as a repeatable friction-regulating and base-restraint bedding layer. The purpose was to simulate, within the steel test frame, the frictional restraint that would normally develop between an infill wall and the supporting RC beam in practical applications. This restraint was necessary to prevent uncontrolled rigid-body sliding of the entire wall base and to promote the intended deformation mechanism, in which relative motion occurs primarily along the horizontal interfaces between brick courses. Cementitious or adhesive bonding materials were not preferred because they could introduce brittle strength limits, require curing time, and increase uncertainty in the test schedule. Visual observations and, where available, image-based displacement measurements confirmed that the lower brick courses remained essentially restrained relative to the supporting beam during IP loading, indicating that the adopted membrane detail successfully provided the intended base boundary condition.

In addition, 20 mm-thick prefabricated expanded polystyrene strips, Styroblok EPS 50 (Styrosan EPS Ürünleri Yalıtım ve Ambalaj Sanayi, Izmir, Türkiye), conforming to EN 13163:2012+A2:2016 [69]) with a nominal density of approximately 12 kg/m^3 were installed within the vertical seismic gaps between the masonry panels and adjacent steel boundary elements. Owing to its characteristically low compressive stress at 10% strain (50 kPa) and highly deformable cellular structure, the EPS material acted primarily as a compressible buffer layer. This layer limited direct stress transfer and prevented premature frame–wall interaction, thereby enabling the structural response of the sliding wall system to be evaluated with minimal influence from unintended boundary restraints.

Where used, a one-component aerosol polyurethane foam, Soudafoam (Soudal Yapı Kimyasalları A.Ş., Istanbul, Türkiye), was utilized to fill the top gap of the wall. The cured semi-rigid material provided a deformable contact medium and partial adhesion, with typical compressive and tensile strengths reported as approximately 0.04 MPa and 0.09 MPa, respectively. Because the material expands after application, the excess foam was trimmed with a utility knife after 1–2 h of curing. In the preliminary configurations, the foam was intended primarily to create a deformable out-of-plane restraint against OOP instability, whereas limiting excessive vertical stress transfer was considered only as a secondary function. Nevertheless, its post-application expansion could have introduced unintended vertical pre-compression on the wall, thereby increasing the normal stress along the sliding interfaces and partly reducing the efficiency of the sliding mechanism. Similar compression effects may also have been amplified under large in-plane drift demands by the slight downward movement of the upper beam of the test frame and by minor dilation associated with the combined sliding–rotation response of the interlocking units. Accordingly, the final detailing strategy aimed to preserve out-of-plane stability while minimizing unintended vertical restraint, particularly near the wall ends.

3.4. Specimen Design and Construction Details

All specimens were constructed using dry-jointed locked bricks made of fired clay, arranged to form discrete horizontal sliding interfaces. No plaster or surface coating was applied to the wall surfaces. The base interface was detailed using the bituminous membrane described in Section 3.3. Two unit geometries were employed, as shown in Figure 2a,b. TB-type units (Vardarlı Tuğla, Turgutlu, Manisa, Türkiye), with dimensions of 250 × 150 × 200 mm (width × height × depth) and a void ratio of 0.5, were used for the thick-wall configurations, representing exterior wall applications. NB-type units (Kudret Tuğla, Turgutlu, Manisa, Türkiye), with dimensions of 190 × 240 × 100 mm and a void ratio of 0.6, were used for the thin-wall configurations, representing interior wall applications.

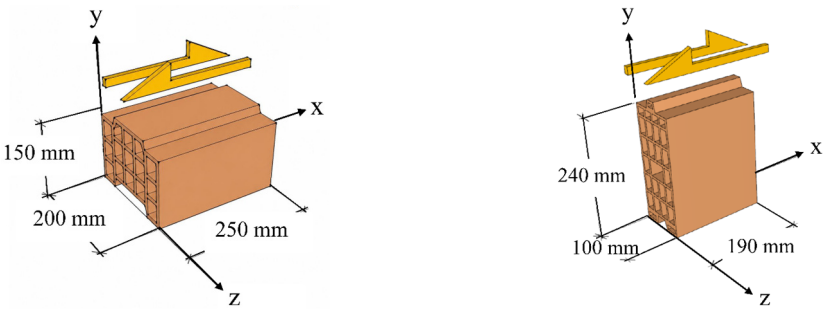

Figure 2. Dimensions of (**a**) TB-type thick units, and (**b**) NB-type thin units, with sliding interface orientation.

The adopted unit geometries resulted in different height-to-depth ratios, directly influencing the balance between sliding and rotational deformation modes. In both configurations, the interlocking arrangement defined continuous horizontal contact planes that facilitated distributed sliding under IP loading. Since no mortar was used between unit layers, the structural response was governed primarily by interface friction and geometric compatibility rather than conventional masonry bonding and cracking mechanisms. This enabled large deformation demands to be accommodated through relative interface motion while limiting damage accumulation within the masonry units.

The window-opening specimens, TW1 and TW2, were constructed using TB-type thick fired-clay units, forming 200 mm-thick walls with fourteen brick courses (Figure 3a,b). A centrally located window opening of 860 × 960 mm (width × height) was framed by 2 mm-thick steel C-sections connected through welded angle-plate rotational connections, formed using 2 mm-thick steel angle pieces welded between adjacent C-section members (Figure 3c–e). These connections were intended to permit local rotation, although limited moment transfer could occur due to their welded configuration. Perforated L-shaped steel profiles fabricated from commercially available 40 × 60 × 2 mm slotted steel shelving profiles (BÜROMSAN Çelik Raf San. ve Tic. Ltd. Şti., Istanbul, Türkiye) were placed along the upper boundary to provide out-of-plane stability, while 20 mm-thick compressible EPS strips were used along the vertical interfaces to prevent direct shear transfer. No polyurethane foam was applied at the top interface; thus, the walls were left vertically unrestrained along the top edge. The vertical seismic gaps were intended to delay direct frame–wall interaction during IP drift, while the intentional top gaps were designed to reduce vertical restraint and limit IP–OOP damage interaction.

The intentional top gap was introduced to reduce vertical restraint and to limit premature compression build-up during IP drift. By preventing early vertical contact between the wall and the upper beam, this detail was intended to reduce unintended frame–wall interaction, suppress compression-diagonal action, and limit local stress concentration near the wall toes. However, leaving the top interface vertically unrestrained also reduces the contribution of conventional vertical arching to OOP resistance. Therefore, the OOP stability of the proposed system was not intended to rely on top contact alone, but on the combined action of interlocking unit geometry, wall thickness, vertical boundary continuity around openings, and local steel restraint elements. The perforated L-shaped steel profiles were used as local lateral retaining elements along the upper boundary and the upper portions of the side boundaries, providing OOP restraint without imposing continuous vertical compression on the wall. Accordingly, the top-gap detail should be interpreted as part of the complete boundary system rather than as an isolated construction feature.

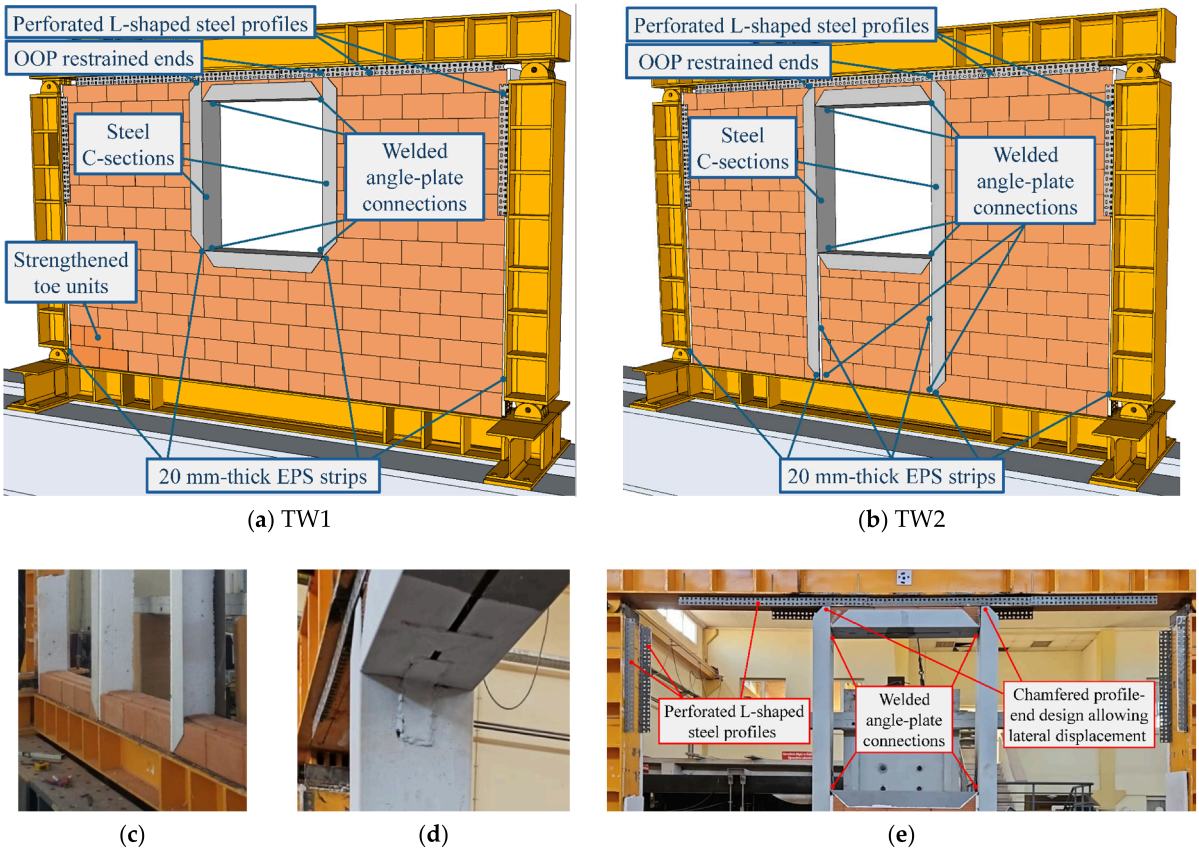

Figure 3. Schematic views of (**a**,**b**) TW1 and TW2 window-opening specimens, (**c**) EPS strip application for TW2 specimen, (**d**) welded angle-plate rotational connection detail, and (**e**) chamfered profile-end design allowing lateral displacement.

The main difference between TW1 and TW2 was the continuity of the vertical window-frame elements. In TW1, these elements terminated above the base beam and were not connected to it. In TW2, they extended over the full wall height and were connected to the base beam through welded angle-plate rotational connections, thereby improving boundary continuity and opening-frame stability. In addition, the lower ends of the vertical frame profiles were chamfered to allow lateral displacement during in-plane deformation. Minor geometric adjustments, including local cutting of brick units, were made where necessary to ensure compatibility between the masonry layout and the frame geometry.

The door-opening specimens, ND1 and ND2, were constructed using NB-type thin fired-clay units, forming 100 mm-thick walls with eight brick courses (Figure 4a,b). A centrally located door opening was framed by 2 mm-thick steel C-sections connected through welded angle-plate rotational connections, formed using 2 mm-thick steel angle pieces welded between adjacent C-section members (Figure 4c). In both specimens, selected units at the wall toes were filled with high-strength repair mortar to improve local compressive resistance; these are referred to as strengthened toe units in the schematic views (Figure 4a,b,d). Two horizontal steel strip elements, referred to as wall ties, were embedded at two elevations to improve out-of-plane stability and limit excessive unit rotation during in-plane deformation (Figure 4e). Along the vertical interfaces between the masonry segments and adjacent steel elements, continuous gaps were filled with 20 mm-thick compressible EPS strips to prevent direct shear transfer. Half-brick units were used where necessary to preserve the staggered brick layout and maintain compatibility with the opening and boundary geometry (Figure 4f).

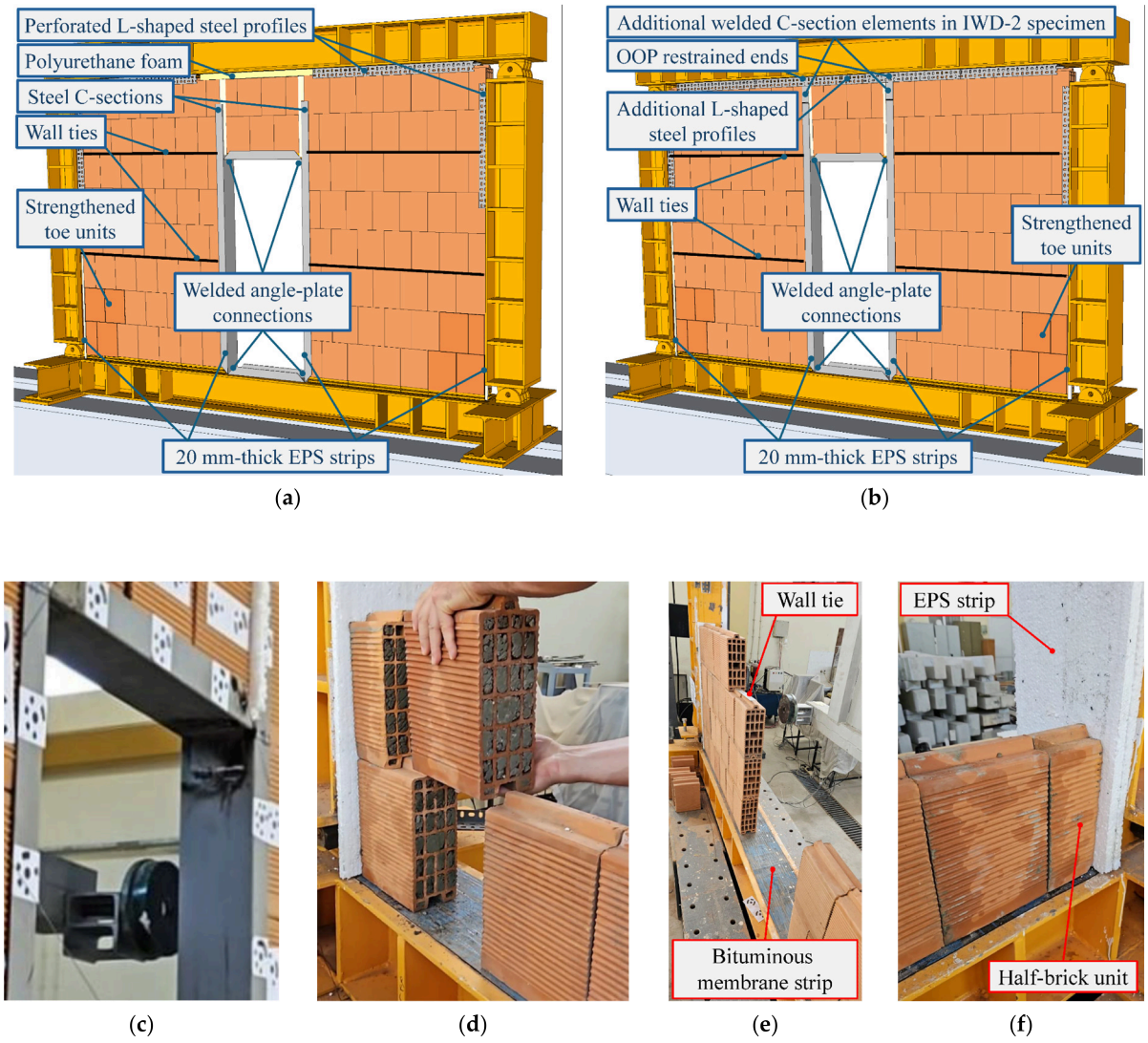

Figure 4. Schematic views of (**a**,**b**) ND1 and ND2 door-opening specimens, (**c**) welded angle-plate connection detail of the door frame, (**d**) strengthened toe units filled with high-strength repair mortar, (**e**) bituminous membrane strip beneath the wall and horizontal wall tie embedded in the wall, and (**f**) half-brick unit used during construction.

The top and side boundary details differed between ND1 and ND2. In ND1, perforated L-shaped steel profiles were placed only along the outer one-third regions of the top beam and the upper one-third regions of the side columns. In the central portion of the top beam, where perforated steel profiles were not used, a localized polyurethane foam layer, restricted to approximately one-fifth of the wall length and centered toward the mid-span region of the top beam, was applied to provide partial deformable out-of-plane restraint while avoiding direct vertical restraint near the wall ends. In ND2, by contrast, perforated L-shaped steel profiles were also used along the central portion of the top beam, extending the upper boundary detailing over the full beam length. Accordingly, no polyurethane foam was applied in ND2.

The main difference between the two specimens was the continuity of the vertical C-sections surrounding the door opening. In ND1, these elements did not extend over the full wall height and were not connected to the top and bottom beams. In ND2, the vertical C-sections extended continuously over the full wall height and were connected to both the top and bottom beams through welded angle-plate rotational connections, thereby enhancing boundary continuity and opening-frame stability.

The steel boundary elements used around the openings were introduced to ensure that the wall segments could deform compatibly with the intended sliding mechanism while preserving OOP stability. In walls with door or window openings, the masonry is divided into interacting subpanels, and the opening frame must therefore accommodate IP drift without forcing the wall into a conventional diagonal compression-strut mechanism. For this reason, the C-section elements surrounding the openings were connected using welded angle-plate rotational connections, which were intended to provide local rotational flexibility while maintaining geometric integrity around the opening. Similar conceptual requirements have also been recognized in previous sliding and unbonded infill systems, where the opening frame must be able to follow the imposed deformation of the surrounding wall segments. The perforated L-shaped steel profiles were used as local OOP restraint elements, particularly near the upper boundary regions where segment instability may develop, whereas the strengthened toe units were introduced to reduce local bearing damage in configurations where vertical restraint or compression concentration could occur. These details inevitably introduce additional fabrication steps compared with a simple bare masonry panel; however, they should be interpreted as proof-of-concept boundary detailing measures for an engineered low-damage infill system. In practical applications, their geometry, continuity, and placement can be further optimized. This additional detailing should also be weighed against the potential savings associated with dry construction, elimination of mortar and plastering, faster installation, and reduced post-earthquake repair demand.

In addition to the specimens with openings, two reference specimens without openings were included to establish baseline structural behavior. The thick-wall reference specimen, TR, and the thin-wall reference specimen, NR, were constructed using TB-type and NB-type units, respectively. Consistent with the corresponding opening specimens, TR consisted of fourteen brick courses, as in TW1 and TW2, whereas NR consisted of eight brick courses, as in ND1 and ND2. The different unit geometries and number of courses resulted in distinct interface distributions and deformation characteristics between the two reference configurations. The vertical seismic gaps between the masonry wall edges and the surrounding steel elements were filled with compressible EPS strips. In TR, the seismic gap width was intentionally varied along the wall height, with 20 mm-thick EPS strips used at the lower courses and 5 mm-thick strips toward the upper region. In the remaining specimens, 20 mm-thick EPS strips were used along the corresponding vertical interfaces.

To improve local compressive resistance, selected units near the wall toes were filled with a high-strength repair mortar in both reference specimens, following the same local toe-strengthening concept adopted in the opening-specimen details shown in Figures 3a and 4a,b. The repair mortar was a commercially available R4-class polymer-modified cementitious repair mortar, Sika MonoTop®-612 (Sika Yapı Kimyasalları A.Ş., Istanbul, Türkiye), containing silica fume and fibers in accordance with EN 1504-3:2005 [70]. These strengthened toe units were intended to increase the local compressive resistance at the wall toes and reduce premature local crushing or bearing damage during cyclic IP deformation.

In NR, additional steel strip elements, 2 mm thick and 20 mm wide, referred to as wall ties, were installed at two elevations corresponding to those shown in Figure 4a,b, to improve stability and limit excessive unit rotation during in-plane deformation. Unlike in ND1 and ND2, however, these steel strip elements were placed continuously along the full wall span.

Out-of-plane stability in both reference specimens was provided by perforated L-shaped steel profiles mechanically fastened to the surrounding steel frame. In both TR and NR, these profiles were placed along the outer one-third regions of the top beam and the upper one-third regions of the side columns, consistent with the boundary detailing

adopted in the opening specimens. However, the top interface restraint conditions differed between the two reference configurations. In TR, a polyurethane foam layer was applied over one-half of the wall length at the top interface, whereas in NR the foam layer was limited to one-third of the wall length, leaving the remaining portions vertically unrestrained. Table 1 summarizes the properties of specimens and the test details.

Table 1. Summary of specimen configurations, boundary details, loading protocols, and availability of image-based results.

Features	Details	Specimens					
		TW1	TW2	ND1	ND2	TR	NR
Opening configuration	Window opening	√	√	-	-	-	-
	Door opening	-	-	√	√	-	-
	No opening	-	-	-	-	√	√
Unit type/wall thickness	TB-type/thick/200 mm	√	√	-	-	√	-
	NB-type/thin/100 mm	-	-	√	√	-	√
Number of brick courses	14	√	√	-	-	√	-
	8	-	-	√	√	-	√
Opening frame	2 mm-thick steel C-sections	√	√	√	√	-	-
Vertical C-section continuity	Full-height vertical C-sections	-	√	-	√	-	-
Wall ties	Installed at two elevations	-	-	√	√	-	√
	Discontinuous at opening region	-	-	√	√	-	-
	Continuous along full wall span	-	-	-	-	-	√
Perforated L-shaped steel profiles	Outer one-third regions of top beam	-	-	√	-	√	√
	Along the full top-beam length	√	√	-	√	-	-
	Upper one-third regions of side columns	√	√	√	√	√	√
Vertical seismic gaps filled with EPS strips	20 mm	√	√	√	√	-	√
	20 mm at lower, 5 mm at upper halves	-	-	-	-	√	-
Polyurethane foam at top interface	One-half of wall length	-	-	-	-	√	-
	One-third of wall length	-	-	-	-	-	√
	One-fifth of wall length	-	-	√	-	-	-
	Not applied	√	√	-	√	-	-
Strengthened toe-units	One toe	√	-	-	-	-	-
	Both toes	-	-	√	√	√	√
	Not applied	-	√	-	-	-	-
Test type	IP	√	√	√	-	√	√
	OOP	√	√	√	√	√	√

Table 1. *Cont.*

Features	Details	Specimens					
		TW1	TW2	ND1	ND2	TR	NR
Image-based results presented in this study	in the IP test	-	-	√	-	-	-
	in the OOP test	√	-	√	√	√	-

Note: √ indicates that the feature is provided; - indicates that the feature is not provided.

3.5. Test Setup, Instrumentation, and Loading Protocol

All specimens were tested within a steel testing frame with a clear internal opening of 3200 × 2000 mm (width × height), defining the effective wall panel dimensions (Figure 1). The frame incorporated pinned joints to minimize moment transfer, while an auxiliary support frame prevented unintended out-of-plane (OOP) motion of the testing system.

In-plane (IP) loading was applied through a hydraulic actuator (TDG, Ankara, Türkiye) connected to the top beam. The applied load was monitored using a 100 kN tension–compression load cell (CAS, Istanbul, Turkey). OOP loading was applied using a separate 100 kN hydraulic actuator (Enerpac, Menomonee Falls, WI, USA) under force-controlled conditions and transmitted to the wall through a four-point loading mechanism. The loading arm included uniaxial hinges allowing rotation about the vertical and horizontal axes, while spherical joints at the spreader-beam ends accommodated local rotations. The load was transferred through semi-rigid plywood plates to ensure distributed application and minimize local stress concentrations.

Conventional measurements were conducted throughout the tests to characterize the structural response and provide reference data for validating the SfM-based measurements. Two separate steel reference frames ensured stable sensor mounting for IP and OOP testing.

IP lateral drifts were monitored using an LVDT (TML, Tokyo Sokki Kenkyujo Co., Ltd., Tokyo, Japan) and a string potentiometer (Opkon Sensör Teknolojileri A.Ş., Istanbul, Turkey) installed between the testing frame and the reference frame at the top level. An additional LVDT monitored possible foundation sliding, while two diagonal string potentiometers measured wall shear deformation (Figure 5).

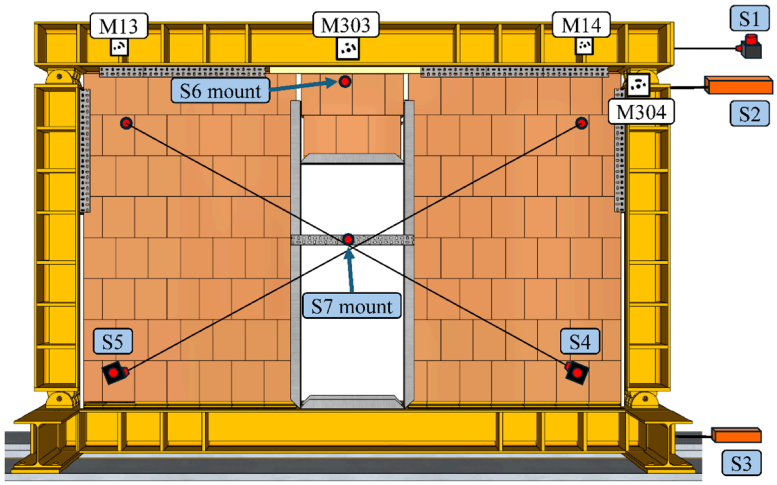

Figure 5. Displacement sensor locations for IP and OOP testing on ND1 specimen.

During OOP tests, the diagonal string potentiometers were repositioned to measure displacements at the wall mid-height and near the top region. The string potentiometers (S1, S4–S7) had a resistance of 10 kΩ, a 900 mm stroke, and ±0.5% linearity, while the

LVDTs (S2–S3) had stroke capacities of 200 mm and 100 mm. All sensors were connected to a TDG1001 data acquisition system (TDG, Izmir, Turkey).

The specimens were subjected to displacement-controlled reversed cyclic IP loading followed by OOP loading. Specimen ND2 was tested only under OOP loading to isolate the influence of boundary detailing without prior IP deformation effects. The IP loading protocol followed ACI 374.2R-13 [71], with three cycles applied at each displacement level. Image acquisition for deformation monitoring was synchronized with discrete top displacement stages of 0, ±35, ±55, and ±80 mm (Figure 6), corresponding to representative deformation levels of sliding wall systems.

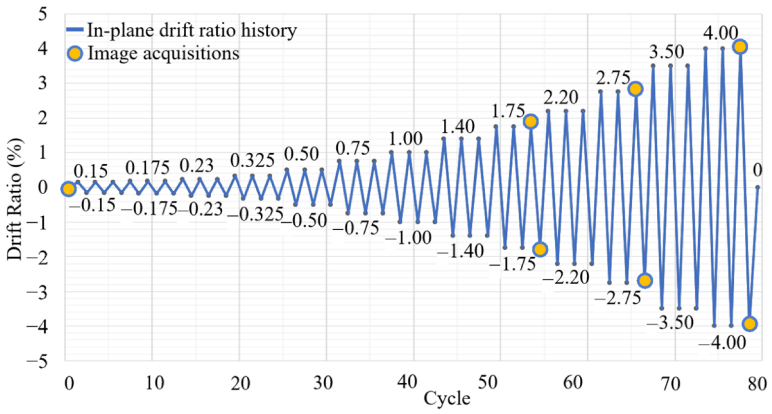

Figure 6. Image acquisition stages along the IP drift history.

Following completion of IP loading, OOP loading was applied under force-controlled conditions. For OOP tests, images were also acquired at the undeformed configuration and at the end of OOP loading corresponding to a significant deformation stage before unloading or instability.

3.6. Image Acquisition and Photogrammetric Processing

Three-dimensional displacements of the wall and testing frame were monitored using a marker-based Structure-from-Motion (SfM) system implemented in Agisoft Metashape [72]. Coded circular markers with unique 14-bit IDs were employed, consisting of two small markers (4.2 cm diameter) per brick and larger markers (6.7 cm diameter) placed at reference points.

In total, 275 markers were distributed across the reference points, testing frame, door/window boundary frame elements, and masonry units, enabling spatially distributed tracking of global and local deformations across successive measurement epochs. The overall marker distribution is illustrated in Figure 7, while selected markers used for validation are indicated in Figure 5.

Images were acquired along a predefined path at an average distance of approximately 4 m (Figure 7c). For each loading stage, approximately 40 images were captured from multiple horizontal positions and vertical levels to ensure robust reconstruction. Camera positions were intentionally varied to improve network geometry and reduce perspective-related errors.

Photogrammetric processing was carried out using Agisoft Metashape and included image alignment, bundle adjustment, automatic coded-marker detection (Figure 7d), and definition of a global coordinate system. Reference marker coordinates were measured prior to testing using a Leica DISTO S910 (Leica Geosystems AG, Heerbrugg, Switzerland) and imported into the photogrammetric environment to establish a stable coordinate framework.

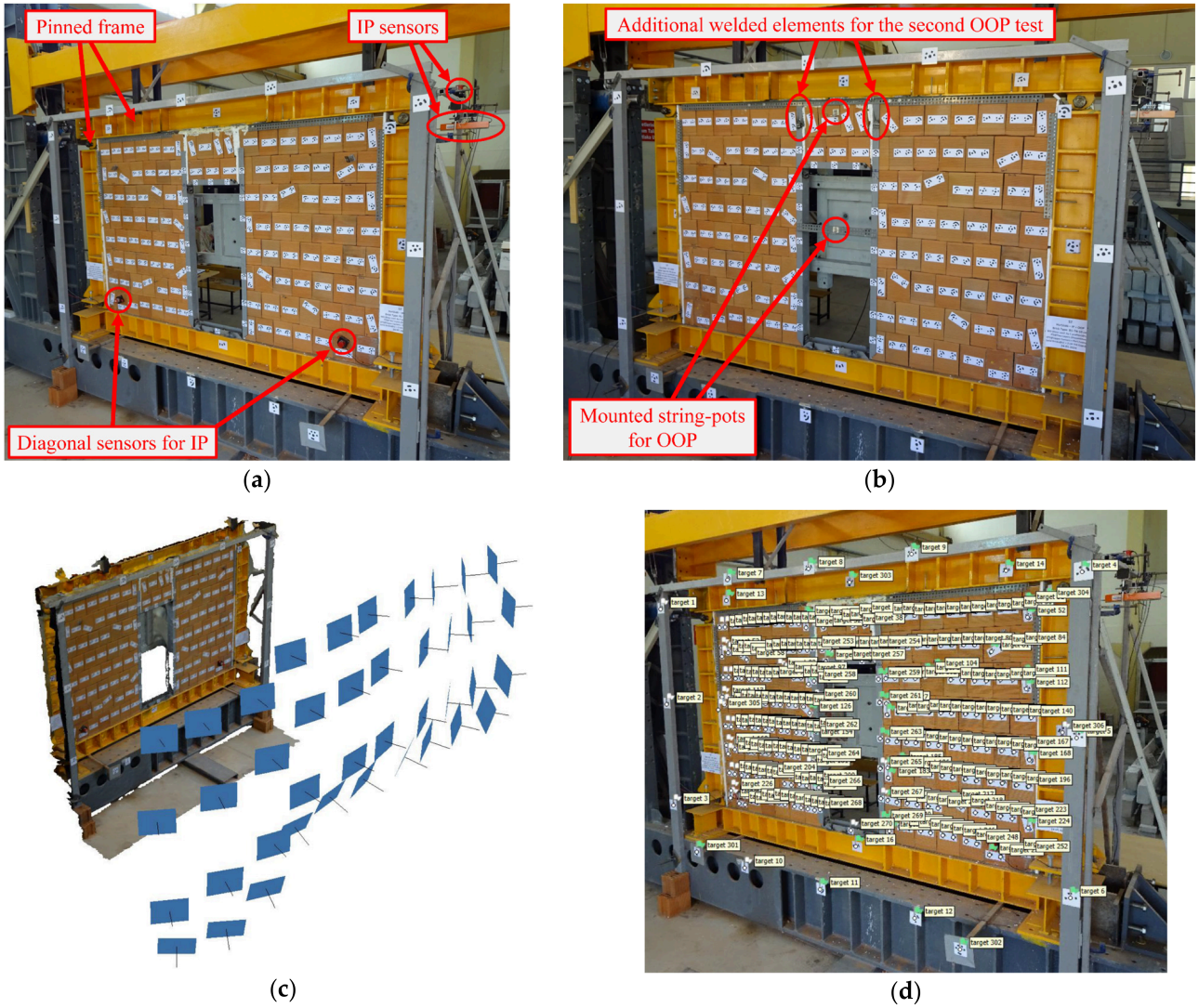

Figure 7. Image acquisition and marker detection procedure: (**a**,**b**) general marker layout on the test specimen and reference elements, (**c**) camera positions used for a single loading stage, and (**d**) automatically detected coded markers shown as target points.

For each loading stage, three-dimensional marker coordinates were reconstructed and displacements were computed relative to the undeformed configuration. The reconstructed marker coordinates were then exported and processed in MATLAB R2024a to compute displacement fields. Both component-wise displacements and resultant displacement magnitudes were calculated from corresponding marker positions across loading stages.

The resulting spatial datasets provide detailed displacement information for both the wall and the testing frame and form the basis for the kinematic and mechanistic interpretation presented in the subsequent sections.

4. In-Plane Response

4.1. Hysteretic Response and Shear Deformation

The IP response of the tested sliding wall specimens was evaluated using top load–drift ratio and average shear stress–shear strain relationships. The comparisons were organized to isolate the effects of wall thickness, opening configuration, and boundary detailing. First, the reference specimens TR and NR were compared to establish the baseline response of the thick- and thin-wall configurations without openings. The thick-wall specimens were then evaluated as a separate group by comparing the thick reference specimen TR

with the window-opening specimens TW1 and TW2, thereby assessing the influence of window openings and vertical boundary continuity. Similarly, the thin-wall specimens were compared within their own group by evaluating the thin reference specimen NR together with the door-opening specimen ND1 to examine the effect of the door opening and associated boundary detailing. ND2 was not included in the IP comparison because it was tested only under OOP loading.

4.1.1. Reference Specimens: TR and NR

The IP response of the reference specimens TR and NR is governed primarily by stable sliding along horizontal interfaces. The direct comparison of the hysteresis curves in Figure 8a highlights the pronounced influence of wall thickness on strength, stiffness, and energy dissipation.

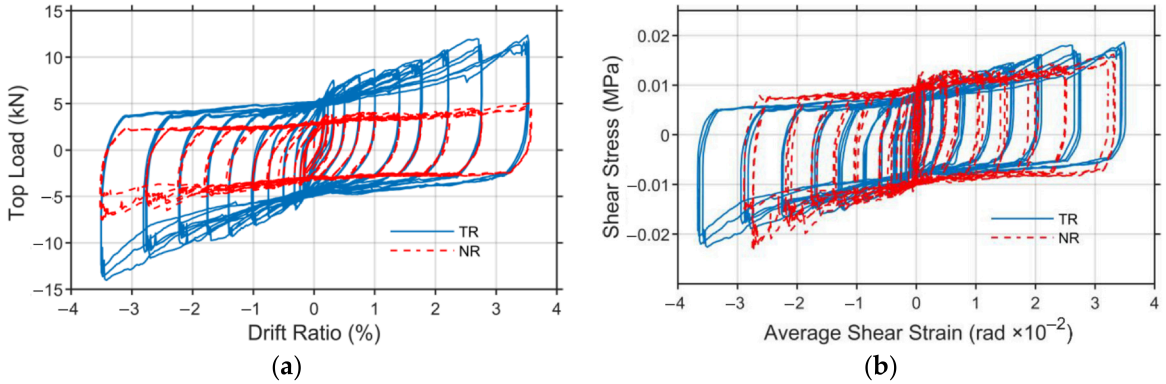

Figure 8. In-plane response of the reference specimens TR and NR: (**a**) top load–drift ratio, and (**b**) average shear stress–shear strain.

TR develops substantially higher lateral resistance, reaching approximately 12–14 kN depending on loading direction at drift levels close to 3.5%. In contrast, NR reaches approximately 5–7.5 kN under comparable drift demands. Its narrower loops, lower initial stiffness, and directional asymmetry reflect the reduced contact area, lower frictional resistance, and greater local rotation in the thinner wall configuration. For both specimens, the friction-type loops remain stable and gradually increase in strength at higher drift levels, indicating progressive mobilization of interface resistance rather than damage-driven softening.

The average shear stress–shear strain responses shown in Figure 8b further support these observations. TR reaches slightly higher positive shear stress, approximately 0.019 MPa, compared with about 0.016 MPa for NR, while both specimens attain similar peak values in the reverse direction, close to 0.023 MPa. The response of NR is more asymmetric and exhibits greater dispersion, particularly in the negative loading direction, reflecting the reduced contact area and increased contribution of local rotation in the thinner wall configuration. Despite these differences, both specimens display similar friction-type loop characteristics, confirming that the governing mechanism remains controlled sliding along horizontal interfaces rather than material cracking.

Visual observations at +3.5% drift further reinforce this interpretation (Figure 9). Both specimens sustain large global deformations without visible cracking, crushing, or fragmentation of the clay units. No continuous compression diagonals or X-shaped cracking patterns are observed. Instead, deformation is distributed along horizontal interfaces, forming a diffuse deformation field rather than a single dominant load path. Unit integrity is preserved, and relative displacements are accommodated through accumulated sliding along multiple interfaces.

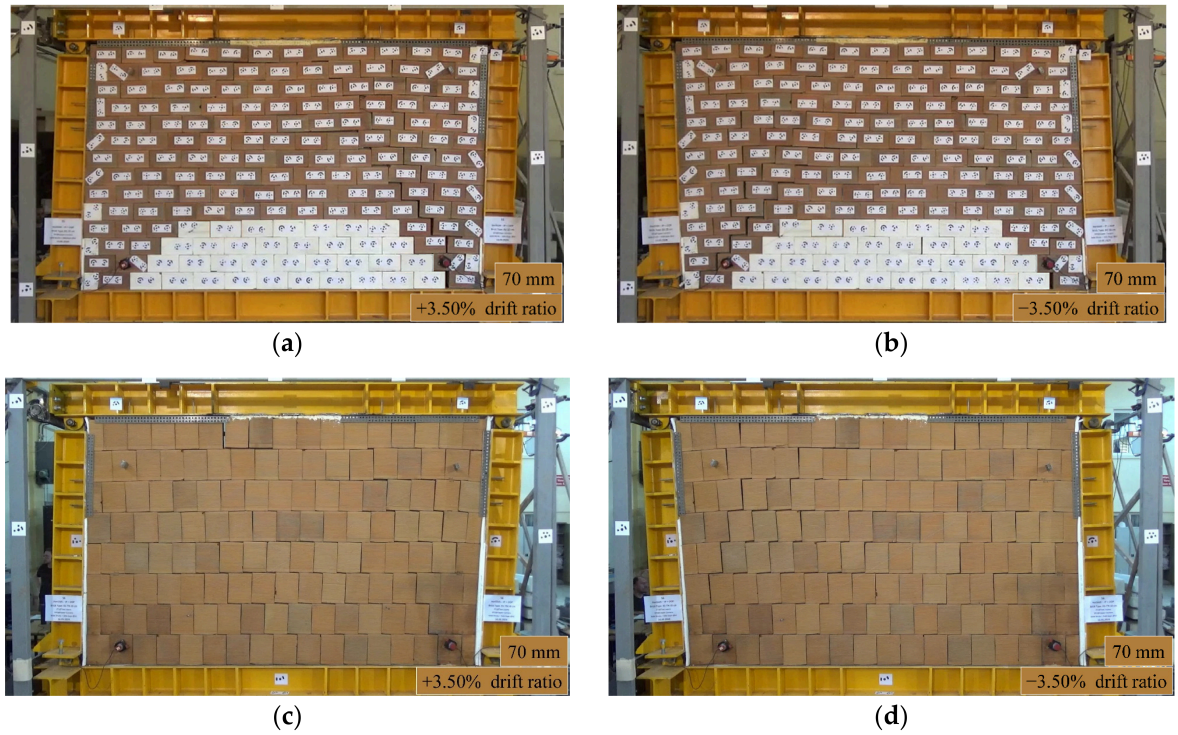

Figure 9. Deformed shapes of the reference specimens (**a**,**b**) TR and (**c**,**d**) NR at ±3.5% drift.

Overall, increasing wall thickness significantly enhances load capacity, stiffness, and shear resistance while preserving the underlying sliding-dominated mechanism. The response is therefore governed by kinematic compatibility and interface interaction rather than by material degradation, reflecting a transition from strength-controlled to deformation-controlled behavior.

4.1.2. Thick-Wall Specimens with Window Opening: TR, TW1, and TW2

The IP response of the thick-wall specimens, including the reference specimen TR and the window-opening specimens TW1 and TW2, highlights the influence of window openings and boundary continuity within a sliding-dominated system. As shown in Figure 10a, all specimens exhibit stable friction-type hysteretic behavior governed by sliding along horizontal interfaces, with no evidence of strength degradation over the imposed drift range.

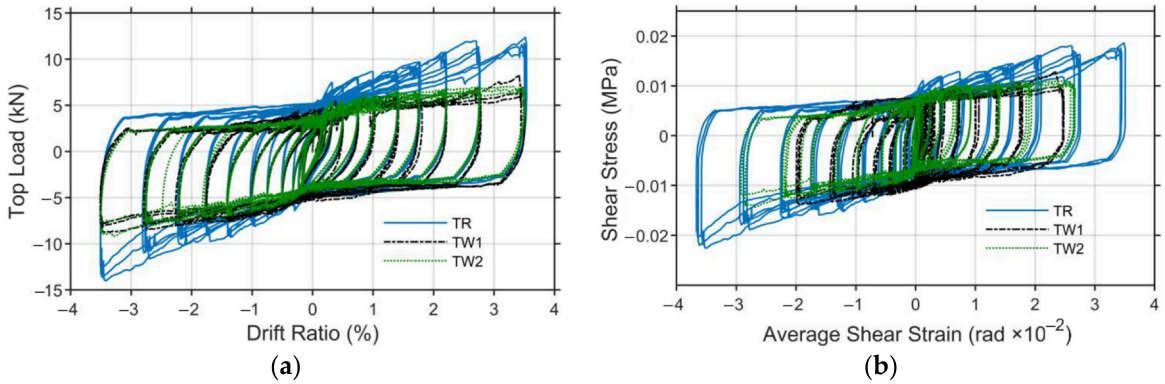

Figure 10. In-plane response of thick-wall specimens TR, TW1, and TW2: (**a**) top load–drift ratio, and (**b**) average shear stress–shear strain.

The TR specimen provides the upper-bound response among the thick-wall configurations, reaching approximately 12–14 kN depending on the loading direction at drift levels close to 3.5%. Its wider and more stable hysteresis loops indicate more effective mobilization of interface friction and load transfer across the full wall panel, without the deformation discontinuities introduced by an opening.

The average shear stress–shear strain relationships in Figure 10b follow the same trend. TR reaches the highest shear stress levels, approximately 0.019 MPa in the positive direction and 0.023 MPa in the reverse direction, while TW1 and TW2 mostly remain within 0.010–0.014 MPa. This reduction indicates lower effective shear-transfer capacity due to the window opening. The average shear strain range is also more limited in TW1 and TW2 than in TR, suggesting that the opening interrupts the continuity of shear deformation and redistributes deformation around the opening region. Nevertheless, all three specimens exhibit comparable friction-type loop shapes, confirming that the response remains governed by sliding along horizontal interfaces rather than transitioning to diagonal strut action or cracking-dominated behavior.

The deformed configurations at ±3.5% drift provide additional evidence of this mechanism (Figure 11). Both TW specimens accommodate large deformations without visible cracking, crushing, or localized damage. No diagonal compression paths or crack localization is observed. Instead, deformation occurs through distributed sliding along horizontal interfaces combined with limited block rotation. TW1 exhibits a more irregular deformation pattern due to reduced boundary continuity, whereas TW2 shows a more uniform and symmetric deformation field, indicating improved kinematic compatibility provided by the continuous vertical frame elements.

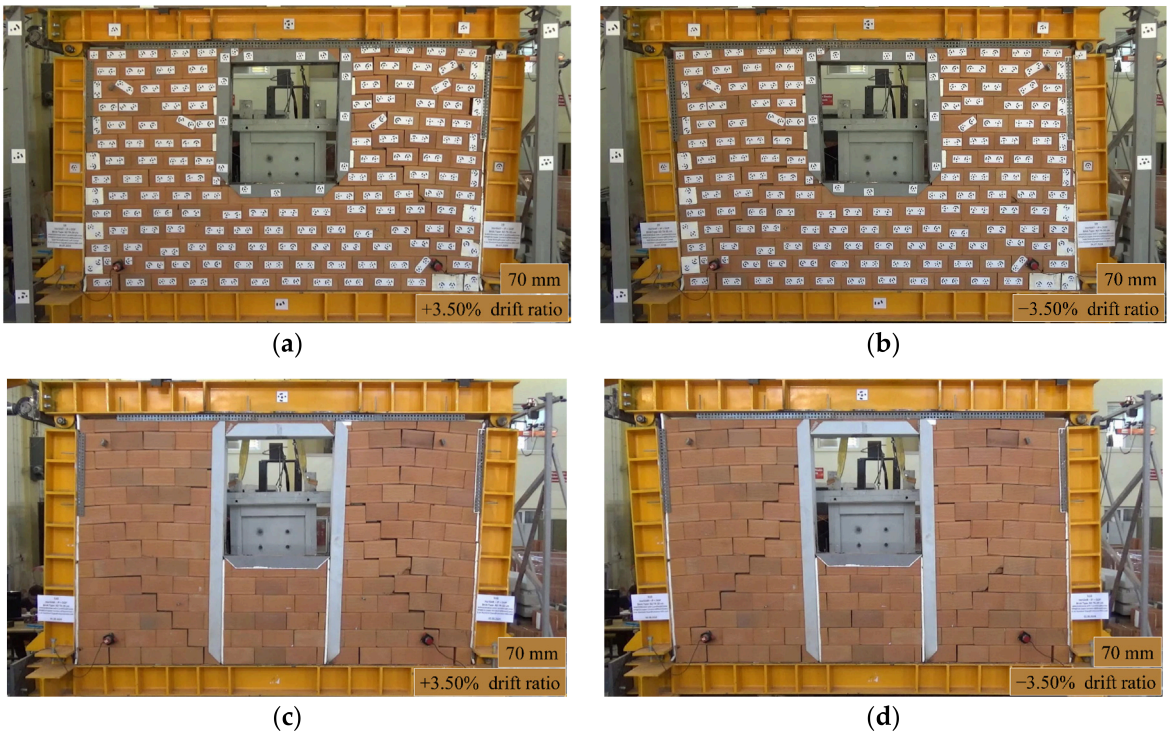

Figure 11. Deformed shapes of (**a**,**b**) TW1 and (**c**,**d**) TW2 specimens at ±3.5% drift.

Overall, the window opening reduces global strength and stiffness relative to the reference thick wall, but it does not alter the sliding-dominated mechanism. Boundary continuity primarily controls the distribution of deformation and improves hysteretic stability.

4.1.3. Thin Wall Specimens with Door Opening: NR and ND1

The IP response of the thin-wall specimens, including the reference specimen NR and the door-opening specimen ND1, demonstrates the influence of wall segmentation on deformation compatibility within a sliding-controlled system. As shown in Figure 12a, both specimens exhibit stable hysteretic behavior governed by frictional sliding, without significant strength degradation over the imposed drift range.

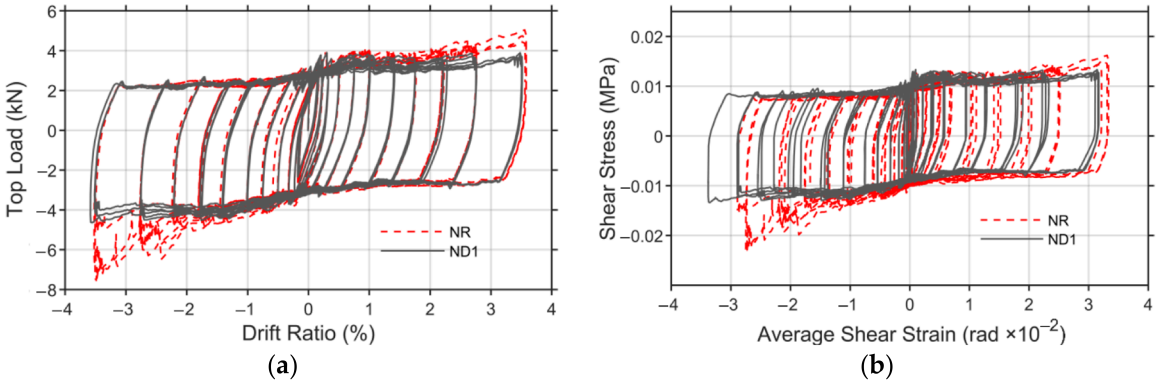

Figure 12. In-plane response of thin-wall specimens NR and ND1: (**a**) top load–drift ratio, and (**b**) average shear stress–shear strain.

The NR specimen reaches peak lateral loads of approximately 5.0 kN in the positive direction and 7.5 kN in the reverse direction, whereas ND1 remains at lower levels of approximately 3.9–4.6 kN under comparable drift demands. This reduction reflects the interruption of load transfer caused by the central door opening, which decreases the effective sliding area and limits continuous load-path development across the wall. The hysteresis loops of ND1 are narrower than those of NR, indicating reduced stiffness and energy dissipation capacity. However, ND1 exhibits a more plateau-like load response at increasing drift levels, whereas the progressive load increase observed in NR suggests increasing resistance mobilization and a greater tendency for unintended contact or compression effects to develop at larger drifts. Overall, both responses remain governed primarily by controlled sliding and segmental deformation rather than damage-driven degradation.

The average shear stress–shear strain relationships shown in Figure 12b further support these observations. ND1 remains within a narrower shear stress range, reaching approximately 0.012–0.013 MPa, whereas NR reaches about 0.016 MPa in the positive direction and locally exceeds 0.020 MPa in the reverse direction. This higher stress demand in NR indicates stronger resistance mobilization at larger deformation levels, which may increase the likelihood of unintended compression or contact effects. In contrast, the more plateau-like response of ND1 suggests that the door opening limits continuous shear-transfer development and promotes a more controlled sliding mechanism. Despite the difference in stress magnitude, both specimens retain similar friction-type loop characteristics, confirming that the response remains governed primarily by sliding along horizontal interfaces.

The deformed configurations provide additional insight into the deformation pattern. Compared with the more uniform deformation field observed in the reference specimen NR (Figure 9), ND1 exhibits clearer segmentation, with two primary wall regions deforming around the opening (Figure 13). Deformation is concentrated along horizontal interfaces within each segment, and increased relative displacement occurs near the opening boundaries. In both specimens, no visible cracking, crushing, or diagonal strut formation is observed; instead, deformation is accommodated through distributed sliding and local interface motion.

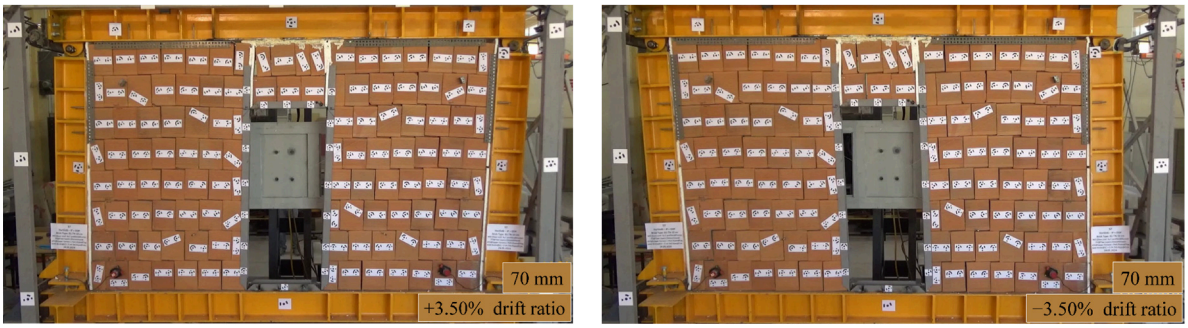

(**a**) (**b**)

Figure 13. Deformed shapes of ND1 under (**a**) push and (**b**) pull loading at ±3.5% drift.

Overall, the introduction of a door opening reduces global strength and modifies deformation compatibility by segmenting the wall. However, it does not alter the fundamental sliding-dominated mechanism. The system continues to sustain large drift demands through distributed sliding rather than material damage.

4.2. Strength, Stiffness, and Energy Dissipation

To complement the interpretation of the hysteretic response, the IP behavior of the specimens was further evaluated in terms of strength envelopes, peak-to-peak secant stiffness degradation, cumulative energy dissipation, and relative energy dissipation ratio. These response parameters provide a quantitative basis for comparing the effects of wall thickness, opening configuration, and boundary continuity on the global response of the sliding wall system.

The strength envelopes were obtained from the peak load values recorded at each drift level in the positive and negative loading directions (Figure 14a). The peak-to-peak secant stiffness was calculated using the load and displacement amplitudes between the positive and negative peak points of each drift level. Energy dissipation was quantified from the enclosed area of each hysteretic loop. In addition, the relative energy dissipation ratio, β, was calculated following the concept described in ACI 374.2R-13 [71] as the ratio of the measured hysteretic loop area to the area of the effective circumscribing parallelograms defined by the initial stiffness and the peak resistance of the corresponding cycle. In the present study, this parameter was not used as an acceptance criterion, but as a normalized index to compare the efficiency of energy dissipation among specimens with different strength and stiffness levels.

The strength envelopes in Figure 14a confirm the trends observed in the hysteretic curves. TR provides the highest lateral resistance in both loading directions, representing the upper-bound response due to its larger wall thickness, contact area, and interface engagement. NR exhibits a considerably lower but stable envelope over the full drift range, reflecting the reduced resistance of the thin-wall reference configuration.

For the thick-wall specimens with window openings, TW1 and TW2 show lower envelope strength than TR because the opening interrupts load transfer across the wall. However, their envelopes remain stable and gradually increase at larger drift levels, indicating that the window reduces resistance magnitude without changing the sliding-dominated mechanism. TW1 develops slightly higher strength in the positive direction at larger drifts, whereas TW2 shows a more balanced bidirectional response, suggesting improved deformation compatibility due to enhanced boundary continuity.

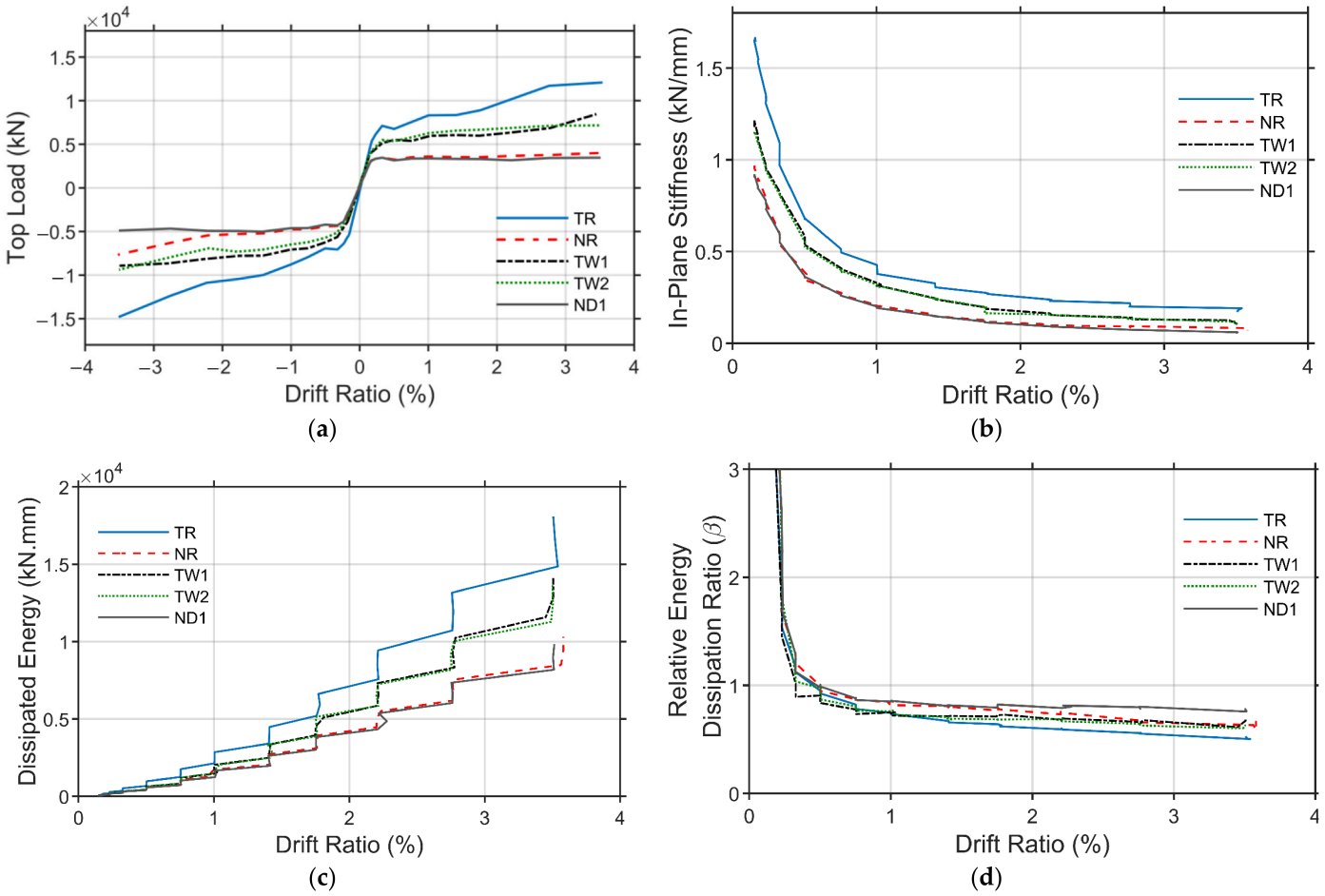

Figure 14. (**a**) Strength envelopes of the IP-tested specimens, (**b**) peak-to-peak secant stiffness degradation curves of the IP-tested specimens, (**c**) cumulative energy dissipation curves of the IP-tested specimens, and (**d**) relative energy dissipation ratio curves of the IP-tested specimens.

For the thin-wall group, ND1 exhibits a lower strength envelope than NR, particularly in the positive loading direction. This reduction reflects the segmentation effect of the central door opening, which decreases the effective sliding area and increases local compatibility demands between wall segments.

The peak-to-peak secant stiffness curves in Figure 14b show a rapid initial decrease for all specimens, followed by gradual degradation and stabilization at larger drift levels. TR exhibits the highest initial stiffness and remains the stiffest specimen throughout the drift range, consistent with its larger wall thickness and more effective inter-unit contact.

TW1 and TW2 show lower stiffness than TR but remain generally stiffer than the thin-wall specimens, indicating that wall thickness has a stronger influence on IP stiffness than the window opening. NR and ND1 exhibit the lowest stiffness values, reflecting the greater flexibility and rotational tendency of the thin-wall configurations; ND1 becomes the least stiff specimen at larger drift levels due to the segmentation effect of the door opening. The absence of abrupt stiffness loss supports the interpretation that deformation is governed by stable sliding and geometric reconfiguration rather than progressive damage accumulation.

The cumulative energy dissipation curves in Figure 14c increase continuously with drift for all specimens, confirming sustained cyclic energy dissipation through repeated sliding. TR dissipates the largest amount of energy, owing to its higher force levels and wider hysteretic loops. TW1 and TW2 follow TR and exhibit similar energy dissipation trends, indicating that the window opening reduces the total dissipated energy relative to the solid thick-wall specimen but does not suppress the sliding-based dissipation mechanism. NR

and ND1 dissipate less energy, consistent with their lower strength and narrower hysteresis loops; the slightly lower response of ND1 reflects the segmentation effect introduced by the door opening.

The relative energy dissipation ratio curves in Figure 14d provide a normalized measure of hysteretic energy dissipation efficiency. In conventional masonry infill systems, cyclic energy dissipation is commonly associated with progressive cracking, corner crushing, and stiffness degradation; therefore, damage-related hysteretic mechanisms may become more pronounced with increasing drift. In contrast, the sliding wall specimens tested in this study exhibit high β values at the initial drift levels, followed by a rapid decrease and stabilization within a relatively narrow range at moderate to large drifts. This trend indicates that, after the initial mobilization of the horizontal sliding interfaces, energy dissipation becomes stable and repeatable, governed primarily by frictional sliding rather than progressive cracking-induced hysteresis. Although the thick-wall specimens dissipate higher absolute energy because of their larger force levels, their relative energy dissipation ratios remain comparable to those of the thin-wall specimens. This suggests that the governing dissipation mechanism is fundamentally similar across the tested configurations, despite differences in wall thickness, opening configuration, and boundary detailing.

Overall, the strength-, stiffness-, and energy-based response parameters indicate that wall thickness primarily controls lateral resistance, initial stiffness, and absolute energy dissipation, whereas openings mainly affect load-transfer continuity and deformation compatibility. Boundary continuity becomes particularly important in specimens with openings, influencing the stability, symmetry, and redistribution of deformation. Despite these configuration-dependent differences, the normalized energy dissipation response suggests that all specimens share a similar governing mechanism, controlled primarily by repeated frictional sliding along the horizontal interfaces rather than progressive damage accumulation.

4.3. Image-Based In-Plane Deformation Analysis

To complement the global measurements and provide spatial insight into the governing deformation mechanisms, image-based measurements were used to reconstruct displacement fields over the wall surface. Rather than focusing on the photogrammetric workflow, which was described in Section 3, this subsection uses the reconstructed marker-based displacement fields to interpret the kinematics of the sliding wall system under IP loading.

The image-based analysis was performed on the ND1 specimen, representing the thin-wall configuration with a central door opening. Displacement data obtained at selected loading stages, including the maximum imposed actuator displacement of ±80 mm, were post-processed to examine horizontal, vertical, and secondary OOP displacement components, as well as displacement-derived deformation indicators. These fields provide direct evidence of how drift demand is accommodated within the wall and around the opening.

Under reversed cyclic IP loading, ND1 exhibited a deformation response fundamentally different from that of conventional masonry infills. Instead of developing a dominant diagonal compression strut, the wall accommodated drift primarily through distributed sliding along horizontal interfaces and localized rotation of brick assemblages. The horizontal displacement fields shown in Figure 15 reveal clear relative motion between the steel testing frame and the infill panel. At the maximum drift level, frame displacements approached the imposed target values, whereas peak wall horizontal displacements remained lower, approximately 65–75 mm. This difference indicates partial kinematic decoupling between the wall and the frame, facilitated by the compressible interface layers along the

vertical boundaries, and confirms that direct force transfer through diagonal compression action was limited.

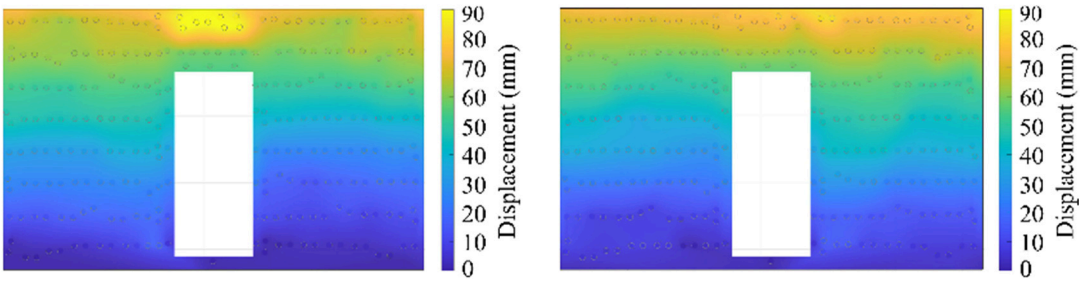

Figure 15. Image-based in-plane horizontal displacement fields of ND1 at maximum drift: (**a**) +80 mm push and (**b**) −80 mm pull.

Deformation was spatially distributed, with sliding activation zones evolving progressively as displacement demand increased. No stable diagonal compression band developed at any drift level. This observation is consistent with the global hysteretic response presented in Sections 4.1 and 4.2, where stable force–displacement loops and limited strength degradation indicated a sliding-controlled mechanism.

Although loading was applied in-plane, measurable vertical and secondary OOP displacement components developed as drift increased. Vertical displacements of brick groups reached approximately 20–25 mm at the largest drift levels (Figure 16). These vertical excursions occurred along inclined zones but did not correspond to compression-dominated cracking bands. Instead, they reflect coupled sliding–rotation kinematics of discrete brick units. Secondary OOP displacements remained moderate, approximately 5–8 mm, but were spatially non-uniform, particularly near the opening boundaries and upper wall regions. The coexistence of horizontal, vertical, and OOP displacement components indicates that the response of sliding infill walls under lateral drift is inherently three-dimensional.

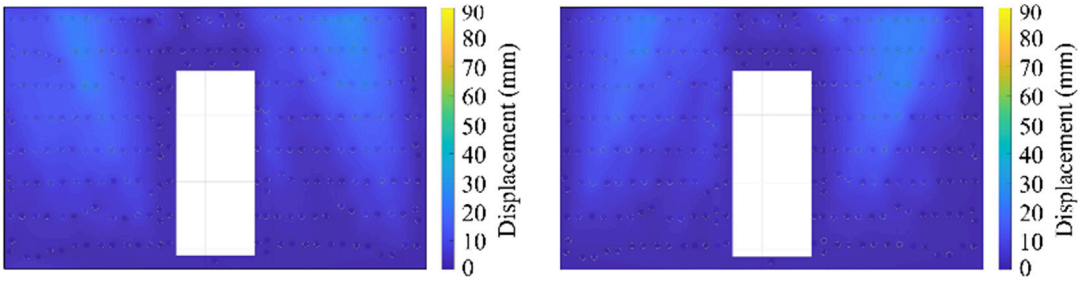

Figure 16. Image-based vertical displacement fields of ND1 at maximum drift: (**a**) +80 mm push and (**b**) −80 mm pull.

This coupled kinematic behavior has practical implications for boundary detailing. In particular, vertical clearances between the infill and the top beam should be sufficient to accommodate combined sliding, uplift, and unit rotation effects. If these movements are unintentionally restrained, premature contact may alter the intended deformation mechanism and increase unintended force transfer to the surrounding frame.

Displacement-derived deformation indicators further support the interpretation of a sliding-dominated mechanism (Figure 17). The normal deformation indicator does not show a persistent narrow diagonal compression band, which would be expected in conventional bonded masonry infills (Figure 17a,b). Instead, moderate deformation values appear in transient and spatially scattered regions, particularly near geometric

discontinuities such as the door opening and upper wall corners. This confirms that IP drift is accommodated primarily through distributed interface activation rather than concentrated crushing-type deformation.

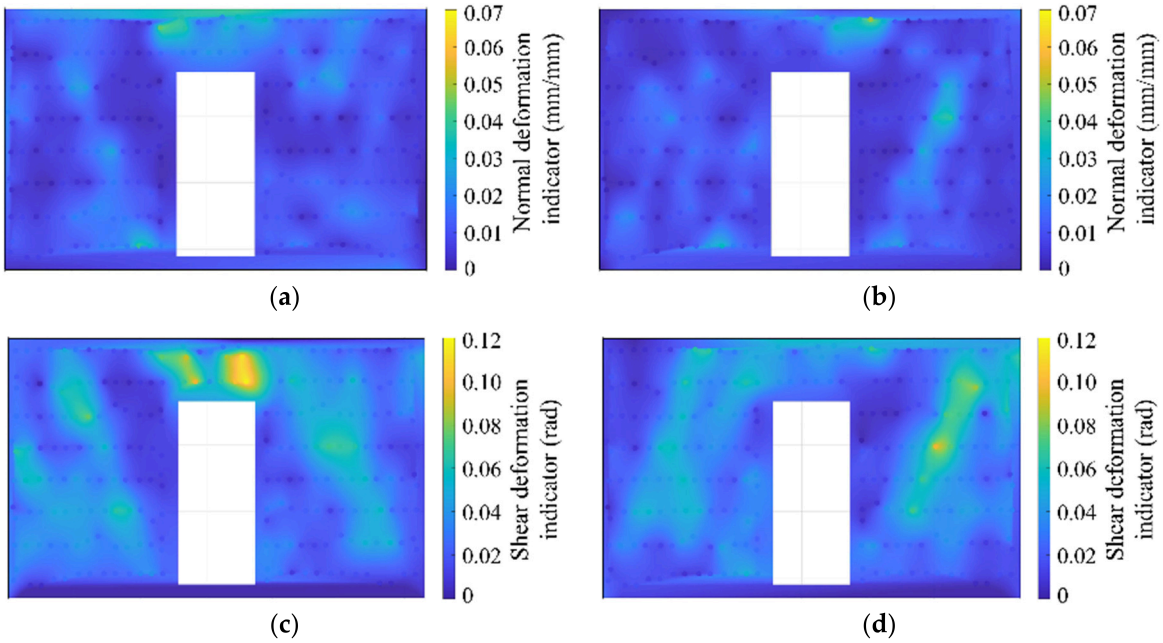

Figure 17. Displacement-derived deformation indicators of ND1: (**a**,**b**) normal deformation indicator and (**c**,**d**) shear deformation indicator at +80 and −80 mm top drift levels, respectively.

The shear deformation indicator reveals progressive activation of sliding interfaces as drift increases (Figure 17c,d). At lower drift levels, deformation remains relatively uniform and compatible. With increasing displacement demand, localized shear concentrations develop near the opening edges and propagate toward the upper courses. However, these concentrations remain spatially diffuse and do not collapse into a single dominant failure band. Similar deformation patterns are observed during push and pull loading, indicating that the sliding and block rotation mechanisms are largely reversible with respect to loading direction.

Overall, the image-based results confirm that the door-opening sliding wall accommodates IP drift through multi-interface sliding, local block rotation, and kinematic compatibility between wall segments rather than through brittle diagonal cracking. These observations provide spatial evidence for the mechanism inferred from the global hysteretic response and support the intended deformation-tolerant design philosophy of the system.

5. Out-of-Plane Response

5.1. OOP Load–Displacement Behavior

The OOP response of the specimens was evaluated using load–displacement relationships obtained from predominantly monotonic OOP tests, including short unloading–reloading segments at selected displacement levels for stiffness evaluation. The comparisons were organized to isolate the effects of wall thickness, opening configuration, and boundary continuity. First, the reference specimens NR and TR were compared to assess the influence of wall thickness. Subsequently, the thick-wall window-opening specimens TW1 and TW2 were evaluated together with TR, while the thin-wall door-opening specimens ND1 and ND2 were compared with NR.

The comparison between the reference specimens NR and TR clearly highlights the dominant influence of wall thickness on OOP load capacity, stiffness, and displacement response (Figure 18a). The TR specimen, reaching approximately 14 kN at about 78 mm, represents an intermediate response in terms of OOP stiffness and load mobilization when compared with the flexible TW1 response and the stiffer boundary-enhanced TW2 response. The load–displacement curve shows nonlinear and stepwise stiffness evolution, reflecting progressive contact engagement between units and redistribution of internal forces as deformation increases. The short unloading–reloading segments observed at selected displacement levels were intentionally applied during testing to evaluate the instantaneous OOP stiffness of the wall and should not be interpreted as sudden strength losses. Overall, TR maintains a stable load-carrying response up to the peak load, indicating effective mobilization of the OOP resistance mechanism.

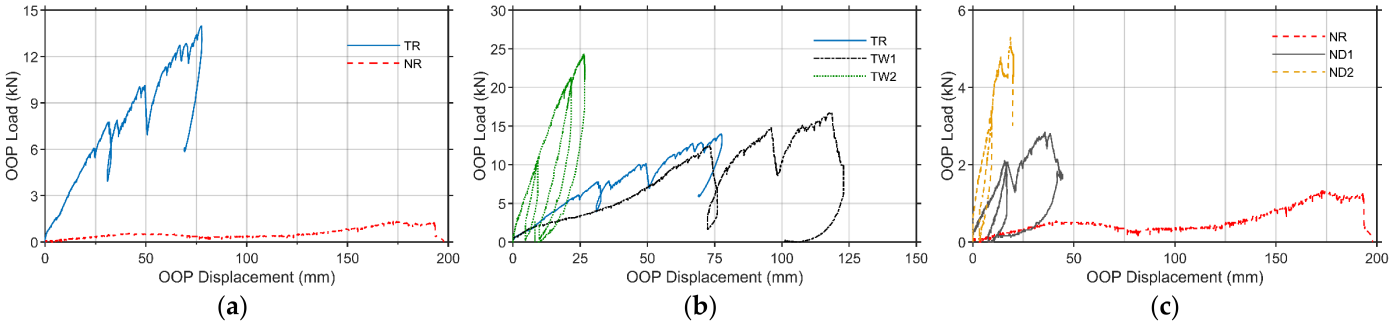

Figure 18. OOP load–displacement relationships of the tested specimens: (**a**) reference specimens (TR and NR), (**b**) thick-wall specimens (TR, TW1, and TW2), and (**c**) thin-wall specimens (NR, ND1, and ND2).

It should be noted that the OOP displacement values reported in this subsection correspond to the point-wise displacement measurements used to construct the load–displacement curves. For the reference specimens without openings, the displacement was measured at the central region of the wall. For the door- and window-opening specimens, the displacement was obtained through reference rods extending from the opening frame toward the representative wall center.

In contrast, the NR specimen exhibits a substantially lower OOP capacity, reaching only about 1.2 kN at much larger displacements of approximately 190 mm. Its response is characterized by an initial low-stiffness increase, followed by a long plateau and only mild load gain at larger displacements. This indicates limited stiffness and delayed mobilization of OOP resistance, consistent with reduced contact interaction and lower confinement in the thin-wall configuration. The strong divergence between NR and TR demonstrates that the OOP behavior of sliding wall systems is governed primarily by wall geometry, contact conditions, and interface engagement. While TR mobilizes significant resistance at relatively small displacements, NR requires large deformation to develop only modest load levels.

The OOP response of the window-opening specimens TW1 and TW2, compared with the reference TR specimen, highlights the combined influence of boundary continuity and deformation compatibility on load transfer mechanisms (Figure 18b). TW1 reaches a peak capacity of approximately 17 kN at a displacement of about 120 mm. Its relatively low initial stiffness and gradual strength development indicate a deformation-controlled response, in which OOP resistance is mobilized progressively through distributed sliding, contact engagement, and large wall deformation. This behavior reflects the flexible response associated with discontinuous vertical boundary elements around the opening.

In contrast, TW2 exhibits the highest OOP capacity, reaching approximately 24 kN at only about 26 mm displacement. The steep initial slope and rapid load development indicate a stiffness-controlled response enabled by continuous vertical boundary elements, which improve load-transfer continuity and constrain relative movement between wall segments. The comparison between TW1 and TW2 shows that boundary continuity not only increases capacity, but also changes how OOP resistance is mobilized: TW1 develops resistance over a large displacement range, whereas TW2 mobilizes higher resistance at much smaller deformation levels. The TR specimen represents an intermediate response between these two boundary conditions.

The OOP response of the door-opening specimens ND1 and ND2, compared with the reference thin-wall specimen NR, shows the strong influence of wall segmentation and boundary continuity on load transfer mechanisms (Figure 18c).

The introduction of a door opening changes this response by subdividing the wall into interacting segments. ND1 reaches approximately 2.8 kN at about 38 mm, indicating a clear increase in stiffness and OOP capacity compared with NR. However, its response still develops over a relatively wide displacement range, suggesting that segmental deformation remains significant. ND2 exhibits a much stiffer response, reaching approximately 5.3 kN at only about 19 mm. This rapid load mobilization reflects the effect of continuous vertical boundary elements, which improve load transfer around the opening and constrain relative movement between wall segments.

Overall, the OOP load–displacement responses demonstrate that wall thickness strongly increases capacity and stiffness, whereas boundary continuity controls whether the response remains flexible and deformation-controlled or shifts toward a stiffer, more capacity-efficient mechanism. Openings influence deformation distribution, but their effect on OOP performance depends primarily on the continuity of vertical load paths and the kinematic compatibility between wall segments. Specimens with improved boundary continuity mobilize resistance at smaller displacements, while discontinuous configurations require larger deformation to develop comparable or lower load levels. Across all specimens, no sudden loss of capacity is observed, indicating progressive force redistribution rather than brittle instability.

5.2. Equivalent Acceleration Capacity and Seismic Demand Perspective

To provide an inertia-based comparison of the measured out-of-plane capacities, the peak OOP loads were normalized by the estimated self-weight of each wall specimen. This normalization provides an equivalent acceleration capacity, a_{cap}, expressed in units of gravitational acceleration:

$$a_{cap} = \frac{F_{OOP,max}}{W} \quad (1)$$

where $F_{OOP,max}$ is the measured peak out-of-plane load and W is the estimated total weight of the wall specimen, including masonry units and steel boundary elements where applicable. This parameter is not intended as a complete code-based design verification, but provides a simple and physically meaningful index for comparing different wall configurations under a common inertia-based reference framework.

The calculated equivalent acceleration capacities are summarized in Table 2. The thin reference specimen NR reached an equivalent acceleration capacity of approximately 0.36 g, whereas the thick reference specimen TR reached approximately 1.78 g, demonstrating the strong influence of wall thickness and unit geometry on OOP resistance. For specimens with openings, the thin-wall group increased from 0.88 g for ND1 to 1.64 g for ND2, indicating that improved vertical boundary continuity nearly doubled the acceleration capacity. In the thick-wall group, TW1 and TW2 reached substantially higher values of approximately 2.38 g and 3.41 g, respectively. The highest value obtained for TW2 reflects the combined

benefit of increased wall thickness, improved contact engagement, and continuous vertical boundary detailing around the window opening.

Table 2. Equivalent acceleration capacities of the tested specimens based on measured OOP peak loads.

Specimen	Configuration	Estimated Weight, (*W*) (kN)	$F_{OOP,max}$ (kN)	a_{cap}
NR	Thin reference wall	3.7	1.32	0.36 g
ND1	Thin wall with door opening	3.22	2.84	0.88 g
ND2	Thin wall with door opening, improved boundary continuity	3.24	5.3	1.64 g
TR	Thick reference wall	7.88	14	1.78 g
TW1	Thick wall with window opening	7.03	16.7	2.38 g
TW2	Thick wall with window opening, improved boundary continuity	7.13	24.29	3.41 g

The results reveal a clear hierarchy in relative OOP resistance expressed by the equivalent acceleration index. Thin-wall specimens without continuous boundary enhancement exhibit lower normalized OOP resistance and rely more strongly on large deformation capacity than on strength. In contrast, thick-wall specimens and boundary-enhanced configurations develop substantially higher acceleration capacity indices, indicating a more efficient resistance mechanism within the adopted quasi-static comparison framework. When the values are considered only as comparative indicators, the thick-wall specimens and the boundary-enhanced thin-wall specimen ND2 show a higher normalized OOP resistance than the thin reference specimen NR and the less boundary-enhanced specimen ND1. However, no direct adequacy judgment with respect to a specific design earthquake is intended. Accordingly, NR should be interpreted as the lowest-resistance configuration, ND1 as an intermediate thin-wall response, and ND2, TR, TW1, and TW2 as configurations with substantially improved normalized OOP resistance due to boundary enhancement, increased wall thickness, or both.

These findings reinforce that the OOP performance of sliding wall systems is governed not only by wall self-weight, but also by unit geometry, wall thickness, contact engagement, and boundary continuity. In particular, continuous vertical boundary elements significantly improve the ability of wall segments to mobilize resistance at smaller displacement levels, shifting the response from a flexible deformation-controlled mode toward a stiffer and more capacity-efficient behavior.

It should be emphasized that the equivalent acceleration capacity adopted herein represents a simplified inertia-based comparison index rather than a complete seismic performance assessment. The parameter does not explicitly account for dynamic amplification, higher-mode effects, frequency-content dependency, record-to-record variability, frame–wall interaction, or cumulative cyclic degradation. Therefore, the calculated values should be interpreted primarily as relative indicators of OOP resistance among the tested wall configurations and not as direct measures of earthquake performance or code-compliance capacity.

A continuous relationship between prior IP drift ratio and residual OOP capacity is not derived in this study because the experimental program did not include repeated OOP tests on identical specimen configurations after different imposed IP drift levels. Such a plot would require a dedicated degradation-type test matrix in which the same wall configuration is subjected to varying levels of prior IP deformation before OOP testing. In

the present program, the OOP capacities reported in Table 2 should therefore be interpreted as configuration-dependent capacities measured after the adopted loading histories, rather than as points on a continuous IP-drift–dependent degradation curve. Moreover, unlike conventional masonry infills, the tested sliding walls did not develop visible cracking, crushing, or diagonal compression strut damage during IP loading; therefore, a conventional IP-damage–induced OOP capacity degradation mechanism was not observed.

The comparison also indicates that the top-gap detail should be evaluated together with the complete boundary configuration. The reference specimens, which did not include vertical C-section subdivision around openings, exhibited lower OOP resistance than the corresponding opening specimens with improved vertical boundary continuity. This suggests that subdividing the wall into narrower interacting strips through opening frames and continuous vertical boundary elements can partly compensate for the reduced contribution of conventional top arching and improve OOP resistance, provided that sufficient boundary compatibility is maintained.

5.3. Image-Based OOP Deformation Fields

Image-based OOP displacement fields were used to complement the global load–displacement responses and to clarify how wall thickness, opening configuration, boundary continuity, and local construction features influence the spatial distribution of deformation. The displacement fields presented in this section correspond to selected stable image-acquisition stages during OOP testing, generally taken before the final load increase leading to peak capacity or instability. Moreover, these marker-based full-field displacement amplitudes represent spatial surface deformations of the wall segments, whereas the OOP displacement values reported in Section 5.1 correspond to point-wise reference measurements used for the load–displacement curves. Therefore, the displacement magnitudes in Sections 5.1 and 5.3 should be interpreted as complementary but not directly identical quantities. The reconstructed fields provide full-field evidence of the deformation mechanisms that cannot be fully captured by point-wise sensors. In this section, the OOP displacement fields of the reference thick-wall specimen TR, the window-opening specimen TW1, and the door-opening specimens ND1 and ND2 are evaluated.

For the reference thick-wall specimen TR, the displacement field exhibits a relatively smooth and symmetric deformation pattern (Figure 19a). The maximum OOP displacement is concentrated near the central region of the wall, reaching approximately 55.5 mm, while displacements gradually decrease toward the vertical and horizontal boundaries. The horizontal and vertical displacement profiles further confirm that deformation is distributed over the wall surface rather than being localized along a narrow deformation band. This behavior is consistent with the progressive OOP load–displacement response of TR, where resistance was mobilized through gradual contact engagement and internal force redistribution. The absence of abrupt deformation localization indicates that the thick reference wall maintained global compatibility and stable OOP behavior.

The TW1 specimen, incorporating a central window opening, exhibits a markedly different deformation pattern (Figure 19b). The displacement field is divided into two main deformation regions on both sides of the opening, with peak values reaching approximately 90–105 mm. The largest OOP displacements occur near the side wall segments adjacent to the opening, whereas the regions directly above and below the opening show different levels of participation. This confirms that the window opening interrupts the continuity of the wall and redistributes deformation toward the remaining wall segments. Compared with TR, TW1 shows a more heterogeneous and flexible deformation field, consistent with its lower initial stiffness and larger displacement demand observed in the OOP load–displacement response. Nevertheless, deformation remains distributed rather than

collapsing into a single localized instability mechanism, indicating that the specimen preserved OOP stability despite large deformations.

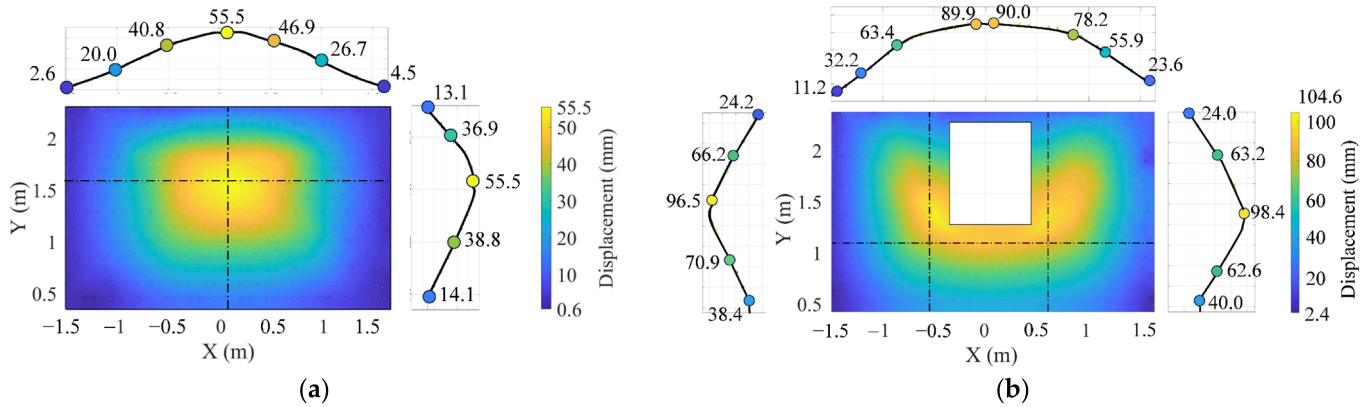

Figure 19. Image-based OOP displacement fields of (**a**) TR and (**b**) TW1.

The comparison between ND1 and ND2 provides direct evidence of the effect of boundary continuity on OOP deformation control (Figure 20). In ND1, the displacement field is strongly asymmetric, with the largest deformation concentrated near the upper region and biased toward one side of the door opening. Peak OOP displacement reaches approximately 84.5 mm, and the vertical side profiles indicate significant differences between the left and right wall segments. This asymmetric deformation pattern is attributed to local flexibility and mobility at the upper connection of the C-shaped door-frame profiles. As a result, one wall segment was allowed to rotate and displace more freely, reducing global stiffness and producing a non-uniform OOP response.

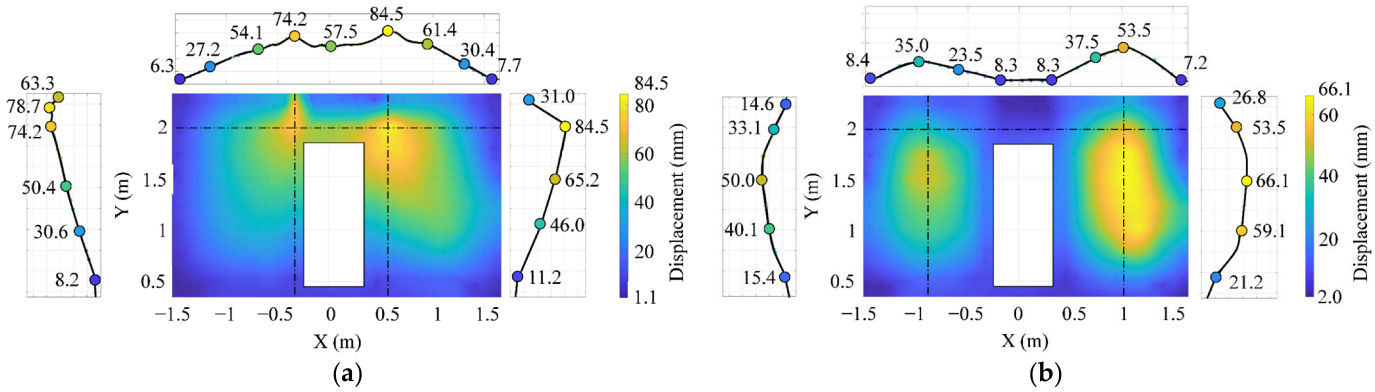

Figure 20. Image-based OOP displacement fields of (**a**) ND1 and (**b**) ND2.

In contrast, ND2 exhibits a more controlled deformation pattern due to improved boundary continuity. The vertical C-profiles at the door edges were extended and connected to the boundary system, which enhanced vertical load-path continuity and local OOP restraint and reduced unintended segmental mobility. Although the maximum displacement in ND2 still reaches approximately 66.1 mm, the deformation field is more clearly separated into controlled side-wall regions with reduced global asymmetry compared with ND1. Together with the higher OOP peak load reported in Section 5.1, this indicates that improved boundary continuity increased stiffness, load-transfer efficiency, and deformation control.

The ND1–ND2 comparison also highlights the role of local construction variability. Even in ND2, where global boundary continuity was improved, the displacement field remains somewhat non-uniform between the two side segments. This suggests that local differences in brick staggering, interlocking efficiency, and segment arrangement can influ-

ence the spatial distribution of OOP deformation. Therefore, while boundary continuity is the dominant parameter controlling global OOP stability, construction quality and masonry arrangement remain important for achieving uniform deformation compatibility.

Overall, the image-based OOP displacement fields support the mechanisms inferred from the global OOP load–displacement curves. The TR specimen shows a smooth and globally compatible deformation mode, TW1 demonstrates distributed deformation around the window opening, and the ND1–ND2 comparison reveals the critical influence of boundary continuity on symmetry, stiffness, and segmental stability. These observations confirm that OOP performance in sliding wall systems is governed not only by wall thickness and opening configuration, but also by the continuity and effectiveness of boundary restraints.

6. Limitations and Future Research

The findings presented in this study are based on a limited number of large-scale experimental specimens specifically designed to investigate the influence of wall thickness, opening configuration, and boundary continuity on the behavior of dry-jointed sliding masonry infills. Although the observed behavioral trends were consistent throughout the experimental program and were informed and corroborated by preliminary experimental development tests conducted before the final specimen series, the investigated parameter space remains limited.

The present study intentionally focuses on experimental characterization and does not attempt to develop a predictive analytical, finite-element, or discrete-element model. Consequently, the proposed deformation mechanisms and load-transfer interpretations should be regarded as experimentally supported behavioral observations rather than generalized predictive formulations. Future studies should address numerical modeling and parametric analyses to evaluate a broader range of geometries, opening ratios, and boundary conditions.

In addition, no repeat tests were performed for individual specimen configurations. As with other large-scale structural testing programs, practical limitations associated with specimen construction, testing time, and cost restricted the possibility of statistical repetition. Nevertheless, the observed trends were consistent with the broader set of preliminary and project-level experimental tests conducted during the development of the system.

The specimens were tested within a steel loading frame to provide repeatable and well-controlled boundary conditions for component-level evaluation of the sliding wall system. The wall panels were not intended to be rigidly integrated with the surrounding frame; direct stress transfer was intentionally limited by EPS-filled vertical seismic gaps, and reduced or eliminated vertical restraint along the top interface. Therefore, the main findings are interpreted primarily as the response of the sliding infill wall system itself rather than as the global response of a specific steel or RC frame. Since the proposed detailing strategy intentionally reduces direct frame–wall interaction through EPS-filled vertical seismic gaps, a controlled base interface, and reduced top restraint, the observed wall-level mechanisms are considered applicable at the component level to RC frame applications in which similar seismic-gap and boundary-detailing conditions are provided. Nevertheless, the influence of RC frame flexibility, beam–column joint deformation, slab restraint, axial load, and frame damage was not included in the present tests and should be investigated in future studies before direct building-level design recommendations are established.

From a practical perspective, the results indicate that the proposed sliding infill concept should be implemented as a combined system rather than as isolated details. The horizontal sliding interfaces and EPS-filled side gaps reduce IP frame–wall interaction and limit

damage accumulation, whereas the results of the tested configurations show that improved OOP stability requires an appropriate combination of wall thickness, unit geometry, and continuous vertical boundary paths, especially around openings. The steel C-sections, L-shaped profiles, welded angle-plate connections, and local toe strengthening used in this study should therefore be interpreted as proof-of-concept boundary detailing measures that can be further simplified and optimized for practical construction. Although these components introduce additional detailing requirements, the dry-jointed system eliminates mortar and plastering operations and may reduce post-earthquake repair demands. Further studies are needed to optimize the detailing, cost, and constructability of the system for real RC frame applications.

Finally, unlike conventional masonry infills, the investigated sliding wall systems developed negligible visible in-plane damage even under large drift demands. Therefore, the primary objective of this study was to quantify the residual OOP response following substantial IP deformation rather than to establish predictive models relating IP damage accumulation to OOP strength degradation. Future research may extend the proposed concept through numerical simulations and seismic loading protocols involving multiple loading histories and dynamic effects.

7. Mechanistic Interpretation and Parametric Effects

A unified interpretation of the experimental results indicates that all specimens were governed by a sliding-dominated mechanism, while wall thickness, opening configuration, and boundary continuity controlled load-transfer efficiency and, consequently, strength, stiffness, deformation capacity, and energy dissipation. Unlike conventional masonry infill walls, where lateral resistance is typically associated with diagonal compression strut formation, cracking, and damage accumulation, the tested systems accommodated deformation mainly through frictional sliding along horizontal interfaces and local rotation of brick assemblages.

For the IP response, openings mainly affected global stiffness and load capacity by interrupting horizontal load paths, without changing the governing deformation mechanism. In thin-wall systems, the door opening reduced strength and introduced segmentation, increasing compatibility demands between adjacent wall regions. In thick-wall systems, window openings similarly reduced IP strength relative to TR. In both cases, the response remained governed by distributed sliding rather than diagonal cracking or compression-strut action.

Wall thickness exerted a dominant influence on IP behavior. Thick-wall specimens developed higher load capacities, stiffness values, and shear stress levels than thin-wall specimens. This can be attributed to increased contact area, improved interlocking efficiency, and reduced unit slenderness, which limited rotational deformation and promoted more effective engagement of the sliding interfaces. By contrast, thin-wall systems exhibited lower strength and stiffness but greater deformation capacity, reflecting a more flexible and distributed kinematic response.

The image-based IP deformation fields further clarify this mechanism. In ND1, displacement maps showed relative motion between the testing frame and the wall, progressive activation of horizontal sliding interfaces, and coupled horizontal, vertical, and secondary OOP displacement components. No stable diagonal compression band was observed, confirming that the IP response was governed by geometric compatibility and interface motion rather than material cracking or compression-strut action.

For the OOP response, wall geometry and boundary detailing became even more influential. The comparison between TR and NR demonstrated the major effect of wall thickness on OOP capacity and stiffness. This difference was associated with increased wall

depth, contact area, unit geometry, and wall assembly. The thick-wall specimens included more brick courses and larger unit depth, improving OOP stiffness, contact engagement, and stability. Conversely, the thin-wall specimens, with fewer courses and more slender units, exhibited delayed resistance mobilization and large displacements under relatively low loads.

The image-based OOP displacement fields support this interpretation. TR exhibited a smooth and relatively symmetric deformation field, with maximum displacement concentrated near the central region and gradually decreasing toward the boundaries, indicating a globally compatible OOP deformation mode. In contrast, TW1 showed a more heterogeneous field, with deformation redistributed toward the side wall segments adjacent to the window opening. This demonstrates that window openings interrupt wall continuity and redistribute OOP deformation while still allowing a stable distributed response.

Boundary continuity governed the transition from flexible, deformation-controlled behavior to a stiffer and more rapidly mobilized OOP response. Specimens without continuous vertical boundary elements, such as ND1 and TW1, exhibited distributed deformation and gradual resistance mobilization. In contrast, ND2 and TW2 developed higher resistance at significantly smaller displacement levels. Thus, boundary continuity not only increased peak capacity, but also changed how resistance was activated and distributed within the wall system.

The OOP image-based comparison between ND1 and ND2 provides direct evidence of this boundary effect. ND1 exhibited a strongly asymmetric displacement field, with deformation concentrated near the upper region and biased toward one side of the door opening, consistent with local mobility of the door-frame C-sections near the upper boundary. ND2 showed a more controlled field, with reduced global asymmetry, confirming that continuous vertical boundary elements improve vertical load-path continuity, local OOP restraint, stiffness, and segmental stability.

Opening configuration further influenced deformation patterns. Door openings promoted localized interaction between the wall regions on either side of the opening, whereas window openings allowed interaction among the wall segments above, below, and beside the opening, leading to a more distributed pattern. In both cases, response effectiveness remained highly sensitive to boundary continuity. The OOP displacement fields also indicate that local construction variability, such as brick staggering and interlocking efficiency, can affect deformation distribution even when global boundary continuity is improved.

The equivalent acceleration capacity assessment further supports these observations as a simplified inertia-based comparison index. Thin-wall configurations without enhanced boundary continuity exhibited relatively low normalized OOP resistance and relied mainly on large deformation capacity. Conversely, thick-wall specimens and boundary-enhanced configurations achieved significantly higher acceleration capacity indices, with TW2 reaching the highest value. This demonstrates that sufficient OOP seismic resistance requires not only a deformable kinematic mechanism, but also adequate wall thickness, unit geometry, contact engagement, and boundary continuity.

Importantly, none of the specimens exhibited brittle failure or sudden loss of capacity during the applied IP or OOP loading stages. For the specimens subjected to sequential IP–OOP loading, the prior IP deformation did not cause visible material degradation that compromised subsequent OOP behavior. This is attributed to the sliding-based IP mechanism, which accommodates drift through largely reversible interface motion rather than cracking. Therefore, unlike conventional infills, where prior IP cracking can substantially reduce OOP stability, the sequentially tested sliding-wall configurations preserved their integrity after large IP drift demands.

The edge details along the vertical supports also contributed to controlling frame–wall interaction during IP drift. The compressible side interfaces delayed direct contact between the surrounding frame and masonry segments, reducing local deformation demand and damage concentration near the vertical boundaries. Combined with the sliding mechanism, these details allowed IP drift to be accommodated through distributed interface motion rather than direct frame-induced compression or cracking.

The intentional top gaps further contributed to reducing unintended IP–OOP interaction by limiting vertical restraint along the upper boundary. This feature becomes important at larger drift levels, where interaction between IP deformation, boundary restraint, and OOP instability may otherwise become more pronounced. However, because reduced top contact may also limit conventional vertical arching contribution, the top-gap detail should be interpreted together with the local OOP restraint elements and vertical boundary continuity, rather than as an isolated stabilizing feature. Thus, the combined use of sliding interfaces, compressible side gaps, top gaps, and local boundary restraint elements reduced IP damage accumulation while preserving OOP stability after imposed IP drift demands.

Across all configurations, the response can be described through three interacting mechanisms: frictional sliding along horizontal interfaces, boundary-controlled load transfer, and geometric compatibility between wall segments. Wall thickness primarily controlled capacity and stiffness, openings governed compatibility demands and deformation redistribution, and boundary continuity determined the effectiveness and symmetry of IP and OOP load transfer. Overall, the results demonstrate that sliding-based masonry wall systems shift the seismic response from damage-controlled resistance to deformation-compatible kinematic behavior, governed primarily by interface mechanics rather than material degradation.

The tested sliding wall concept therefore highlights two key advantages over conventional infill wall systems. First, the sliding interfaces and compressible side gaps reduce IP damage accumulation by allowing drift accommodation through distributed kinematic motion. Second, the combined top-gap and local restraint strategy reduces unintended IP–OOP interaction while maintaining OOP stability through dedicated boundary detailing.

8. Conclusions

This study investigated the in-plane (IP) and out-of-plane (OOP) behavior of full-scale dry-jointed sliding masonry wall systems with varying wall thickness, opening configuration, and boundary detailing. Global hysteretic response, stiffness degradation, energy dissipation, OOP load-carrying capacity, equivalent acceleration capacity, and image-based deformation fields were jointly evaluated. Based on the experimental results and mechanistic interpretation, the following conclusions can be drawn:

1. The tested specimens exhibited a sliding-dominated response mechanism, in which deformation was accommodated mainly through frictional sliding along horizontal interfaces and local rotation of brick assemblages, rather than material cracking or crushing. Even at drift levels up to approximately 3.5%, no stable diagonal compression strut, X-shaped cracking pattern, or brittle failure mode was observed, indicating a fundamental departure from the damage-based behavior of conventional masonry infill walls.
2. Under IP loading, the specimens exhibited stable hysteretic behavior with limited strength degradation. The strength envelopes and peak-to-peak secant stiffness curves showed gradual stiffness reduction rather than abrupt resistance loss, confirming that the response was governed by progressive interface mobilization and geometric reconfiguration.

3. Wall thickness was a dominant parameter controlling IP strength, stiffness, and shear resistance. The thick reference specimen TR developed substantially higher lateral capacity and stiffness than the thin reference specimen NR, mainly due to increased contact area, reduced unit slenderness, and more effective engagement of the sliding interfaces. Nevertheless, both thin- and thick-wall specimens preserved the same sliding-controlled deformation mechanism.
4. Openings primarily affected deformation compatibility and global stiffness rather than altering the governing mechanism. The door opening in ND1 segmented the thin wall into two interacting regions and reduced IP capacity, while the window openings in TW1 and TW2 reduced the effective load-transfer area of the thick-wall configuration. In all opening configurations, the response remained stable and sliding-dominated.
5. Energy dissipation was governed by repeated frictional sliding along horizontal interfaces rather than cracking-induced hysteresis. Thick-wall specimens dissipated greater cumulative energy because of their higher force levels, whereas the relative energy dissipation ratios indicated that the fundamental dissipation mechanism remained comparable across the tested configurations. The absence of a pronounced large-drift increase in relative energy dissipation further supports the interpretation of stable interface sliding rather than progressive damage accumulation.
6. Image-based IP deformation fields provided direct spatial evidence of the intended kinematic mechanism. For ND1, displacement maps showed partial kinematic decoupling between the testing frame and the wall, progressive activation of horizontal sliding interfaces, and coupled horizontal, vertical, and secondary OOP displacement components. No stable diagonal compression band developed, confirming the deformation-tolerant design philosophy of the system.
7. Under OOP loading, wall thickness and boundary continuity strongly controlled stiffness, load capacity, and displacement response. TR reached approximately 14 kN, whereas NR remained below approximately 1.5 kN while undergoing much larger displacements. Boundary continuity was particularly critical for specimens with openings: ND2 reached approximately 5.3 kN compared with approximately 2.8 kN for ND1, while TW2 reached approximately 24.3 kN, exceeding both TW1 and TR. These results show that continuous vertical boundary elements can shift the OOP response from a flexible, deformation-controlled mode to a stiffer and more rapidly mobilized resistance mechanism.
8. The equivalent acceleration capacity assessment provided a simplified inertia-based comparison of the measured OOP capacities, with values ranging from approximately 0.36 g for NR to 3.41 g for TW2. Thin-wall specimens without enhanced boundary continuity relied mainly on deformation capacity, whereas thick-wall and boundary-enhanced configurations developed substantially higher acceleration capacity indices. These values should be interpreted as relative indicators of normalized OOP resistance rather than direct measures of earthquake performance or code-level seismic adequacy. The results indicate that improved OOP resistance requires not only sliding capability, but also adequate wall thickness, unit geometry, and effective boundary continuity.
9. Image-based OOP displacement fields confirmed the mechanisms inferred from the global load–displacement responses. TR exhibited a smooth and globally compatible deformation pattern, TW1 showed deformation redistribution around the window opening, and the ND1–ND2 comparison demonstrated that improved boundary continuity reduced asymmetric segmental deformation. The results also indicate that local construction variability, including brick staggering and interlocking efficiency, can influence the spatial distribution of OOP deformation.

10. For the specimens subjected to sequential IP–OOP loading, prior IP deformation did not cause brittle damage or sudden loss of subsequent OOP stability. The sliding-based IP mechanism, together with compressible side gaps and intentional top gaps, reduced frame–wall interaction and helped separate IP and OOP response mechanisms. As a result, deformation was accommodated in a largely reversible, kinematic manner rather than through critical material degradation. This contrasts with conventional masonry infill systems, where IP cracking can substantially reduce subsequent OOP stability and increase the risk of OOP dropout.
11. Overall, the findings demonstrate that sliding-based masonry wall systems with openings represent a shift from damage-controlled resistance to deformation-compatible seismic behavior. Their performance is governed primarily by kinematic adaptability, interface mechanics, and boundary-controlled load transfer rather than material degradation. While the sliding mechanism effectively enhances drift accommodation and limits damage accumulation, adequate OOP seismic resistance also requires appropriate wall thickness, unit geometry, and boundary continuity.

Author Contributions: Conceptualization, I.S.M., A.C.D. and S.C.G.; Methodology, I.S.M. and A.C.D.; Software, A.C.D. and O.O.; Validation, I.S.M., A.C.D. and O.O.; Formal Analysis, I.S.M. and A.C.D.; Investigation, I.S.M., A.C.D., O.O. and C.C.; Resources, I.S.M., S.C.G., O.O.; Data Curation, I.S.M. and A.C.D.; Writing—Original Draft Preparation, I.S.M. and A.C.D.; Writing—Review & Editing, I.S.M., A.C.D., S.C.G., O.O. and C.C.; Visualization, I.S.M. and A.C.D.; Supervision, I.S.M.; Project Administration, I.S.M.; Funding Acquisition, I.S.M. All authors have read and agreed to the published version of the manuscript.

Funding: This research was funded by the Turkish Council of Higher Education Research Universities Support Program (YOK-ADEP), Grant No. FBA-2023-3063.

Data Availability Statement: The original contributions presented in the study are included in the article, further inquiries can be directed to the corresponding author.

Acknowledgments: This work was supported by the Dokuz Eylül University Scientific Research Projects Coordination Unit under the project entitled "Development of Safe Application Details for Sliding Infill Walls in Reinforced Concrete Frames and Evaluation of Strength-Based Seismic Design Parameters" (Project Number: FBA-2023-3063). The authors gratefully acknowledge the support of the Structural Engineering Laboratory of Dokuz Eylül University, where all experimental tests were conducted, and TUKDER for providing material and workmanship support during specimen construction. The authors also thank Serdar Savtuna, Ibrahim Diboglu, Ersen Kose, Sena Karakaya, and Emirhan Kuzu for their dedicated assistance during the experimental program.

Conflicts of Interest: The authors declare no conflicts of interest. The funders had no role in the design of the study; in the collection, analyses, or interpretation of data; in the writing of the manuscript; or in the decision to publish the results.

References

1. Fardis, M.N.; Panagiotakos, T.B. Seismic design and response of bare and masonry-infilled reinforced concrete buildings part II: Infilled structures. *J. Earthq. Eng.* **1997**, *1*, 475–503. [CrossRef]
2. Madan, A.; Reinhorn, A.M.; Mander, J.B.; Valles, R.E. Modeling of masonry infill panels for structural analysis. *J. Struct. Eng.* **1997**, *123*, 1295–1302. [CrossRef]
3. Negro, P.; Colombo, A. Irregularities induced by nonstructural masonry panels in framed buildings. *Eng. Struct.* **1997**, *19*, 575–585. [CrossRef]
4. Chrysostomou, C.Z.; Asteris, P.G. On the in-plane properties and capacities of infilled frames. *Eng. Struct.* **2012**, *41*, 385–402. [CrossRef]
5. Dias-Oliveira, J.; Rodrigues, H.; Asteris, P.G.; Varum, H. On the seismic behavior of masonry infilled frame structures. *Buildings* **2022**, *12*, 1146. [CrossRef]

6. Sezen, H.; Whittaker, A.S.; Elwood, K.J.; Mosalam, K.M. Performance of reinforced concrete buildings during the August 17, 1999 Kocaeli, Turkey earthquake, and seismic design and construction practise in Turkey. *Eng. Struct.* **2003**, *25*, 103–114. [CrossRef]
7. Vicente, R.S.; Rodrigues, H.; Varum, H.; Costa, A.; Mendes da Silva, J.A.R. Performance of masonry enclosure walls: Lessons learned from recent earthquakes. *Earthq. Eng. Eng. Vib.* **2012**, *11*, 23–34. [CrossRef]
8. Varum, H.; Furtado, A.; Rodrigues, H.; Dias-Oliveira, J.; Vila-Pouca, N.; Arêde, A. Seismic performance of the infill masonry walls and ambient vibration tests after the Ghorka 2015, Nepal earthquake. *Bull. Earthq. Eng.* **2017**, *15*, 1185–1212. [CrossRef]
9. Yakut, A.; Sucuoğlu, H.; Binici, B.; Canbay, E.; Donmez, C.; İlki, A.; Caner, A.; Celik, O.C.; Ay, B.Ö. Performance of structures in İzmir after the Samos island earthquake. *Bull. Earthq. Eng.* **2022**, *20*, 7793–7818. [CrossRef] [PubMed]
10. Gurbuz, T.; Cengiz, A.; Kolemenoglu, S.; Demir, C.; Ilki, A. Damages and failures of structures in Izmir (Turkey) during the October 30, 2020 Aegean Sea earthquake. *J. Earthq. Eng.* **2023**, *27*, 1565–1606. [CrossRef]
11. Doğan, T.P.; Kalkan, H.; Aldemir, Ö.; Ayhan, M.; Böcek, M.; Anıl, Ö. Investigation of RC structure damages after February 6, 2023, Kahramanmaraş earthquake in the Hatay region. *Bull. Earthq. Eng.* **2024**, *22*, 5201–5229. [CrossRef]
12. Taghavi, S.; Miranda, E. *Response Assessment of Nonstructural Building Elements*; PEER Report No. 2003/05; Pacific Earthquake Engineering Research Center: Berkeley, CA, USA, 2003.
13. Filiatrault, A.; Sullivan, T. Performance-based seismic design of nonstructural building components: The next frontier of earthquake engineering. *Earthq. Eng. Eng. Vib.* **2014**, *13*, 17–46. [CrossRef]
14. Mehrabi, A.B.; Shing, P.B.; Schuller, M.P.; Noland, J.L. Experimental Evaluation of Masonry-Infilled RC Frames. *J. Struct. Eng.* **1996**, *122*, 228–237. [CrossRef]
15. Crisafulli, F.J. Seismic Behaviour of Reinforced Concrete Structures with Masonry Infills. Ph.D. Thesis, University of Canterbury, Christchurch, New Zealand, 1997.
16. Asteris, P.G.; Kakaletsis, D.J.; Chrysostomou, C. Failure modes of in-filled frames. *Electron. J. Struct. Eng.* **2011**, *11*, 11–20. [CrossRef]
17. Calvi, G.M.; Bolognini, D. Seismic response of reinforced concrete frames infilled with weakly reinforced masonry panels. *J. Earthq. Eng.* **2001**, *5*, 153–185. [CrossRef]
18. Angel, R.; Abrams, D.P.; Shapiro, D.; Uzarski, J.; Webster, M. *Behavior of Reinforced Concrete Frames with Masonry Infills*; Civil Engineering Studies, Structural Research Series No. 589; University of Illinois Engineering Experiment Station: Urbana-Champaign, IL, USA, 1994.
19. Abrams, D.P.; Angel, R.; Uzarski, J. Out-of-plane strength of unreinforced masonry infill panels. *Earthq. Spectra* **1996**, *12*, 825–844. [CrossRef]
20. Flanagan, R.D.; Bennett, R.M. Bidirectional behavior of structural clay tile infilled frames. *J. Struct. Eng.* **1999**, *125*, 236–244. [CrossRef]
21. Misir, I.S.; Ozcelik, O.; Girgin, S.C.; Yucel, U. The behavior of infill walls in RC frames under combined bidirectional loading. *J. Earthq. Eng.* **2016**, *20*, 559–586. [CrossRef]
22. Ricci, P.; Di Domenico, M.; Verderame, G.M. Experimental investigation of the influence of slenderness ratio and of the in-plane/out-of-plane interaction on the out-of-plane strength of URM infill walls. *Constr. Build. Mater.* **2018**, *191*, 507–522. [CrossRef]
23. De Risi, M.T.; Di Domenico, M.; Ricci, P.; Verderame, G.M.; Manfredi, G. Experimental investigation on the influence of the aspect ratio on the in-plane/out-of-plane interaction for masonry infills in RC frames. *Eng. Struct.* **2019**, *189*, 523–540. [CrossRef]
24. Demirel, I.O.; Binici, B.; Yakut, A. In-plane seismic performance of different infill wall systems in ductile reinforced concrete frames. *Bull. Earthq. Eng.* **2023**, *21*, 3433–3459. [CrossRef]
25. Halici, O.F.; Demir, U.; Zabbar, Y.; Ilki, A. Out-of-plane seismic performance of bed-joint reinforced Autoclaved Aerated Concrete (AAC) infill walls damaged under cyclic in-plane displacement reversals. *Eng. Struct.* **2023**, *286*, 116077. [CrossRef]
26. Zhang, M.; Ding, K.; Pang, L.; Ding, J. In-plane/out-of-plane seismic performance of masonry infilled RC frame structure made of nano-SiO2 reinforced mortar: Experimental study. *J. Build. Eng.* **2023**, *68*, 106104. [CrossRef]
27. Mosalam, K.M.; White, R.N.; Gergely, P. Static response of infilled frames using quasi-static experimentation. *J. Struct. Eng.* **1997**, *123*, 1462–1469. [CrossRef]
28. Kakaletsis, D.J.; Karayannis, C.G. Influence of masonry strength and openings on infilled R/C frames under cycling loading. *J. Earthq. Eng.* **2008**, *12*, 197–221. [CrossRef]
29. Stavridis, A.; Shing, P.B. Finite-element modeling of nonlinear behavior of masonry-infilled RC frames. *J. Struct. Eng.* **2010**, *136*, 285–296. [CrossRef]
30. Misir, I.S.; Ozcelik, O.; Girgin, S.C.; Kahraman, S. Experimental work on seismic behavior of various types of masonry infilled RC frames. *Struct. Eng. Mech.* **2012**, *44*, 763–774. [CrossRef]
31. Misir, I.S. Potential use of locked brick infill walls to decrease soft-story formation in frame buildings. *J. Perform. Constr. Facil.* **2015**, *29*, 04014133. [CrossRef]

32. Karadogan, F.; Pala, S.; Ilki, A.; Yuksel, E.; Mowrtage, W.; Teymur, P.; Erol, G.; Taskin, K.; Comlek, R. Improved infill walls and rehabilitation of existing low-rise buildings. In *Seismic Risk Assessment and Retrofitting: With Special Emphasis on Existing Low Rise Structures*; Springer: Dordrecht, The Netherlands, 2009; pp. 387–426. [CrossRef]
33. Koutas, L.N.; Bournas, D.A. Out-of-plane strengthening of masonry-infilled RC frames with textile-reinforced mortar jackets. *J. Compos. Constr.* **2019**, *23*, 04018079. [CrossRef]
34. De Risi, M.T.; Furtado, A.; Rodrigues, H.; Melo, J.; Verderame, G.M.; Arêde, A.; Manfredi, G. Influence of textile reinforced mortars strengthening on the in-plane/out-of-plane response of masonry infill walls in RC frames. *Eng. Struct.* **2022**, *254*, 113887. [CrossRef]
35. Riddington, J.R. The influence of initial gaps on infilled frame behaviour. *Proc. Inst. Civ. Eng.* **1984**, *77*, 295–310. [CrossRef]
36. Gams, M.; Kwiecień, A.; Korelc, J.; Rousakis, T.; Viskovic, A. Modelling of deformable polymer to be used for joints between infill masonry walls and RC frames. *Procedia Eng.* **2017**, *193*, 455–461. [CrossRef]
37. Tsantilis, A.V.; Triantafillou, T.C. Innovative seismic isolation of masonry infills using cellular materials at the interface with the surrounding RC frames. *Eng. Struct.* **2018**, *155*, 279–297. [CrossRef]
38. Marinković, M.; Butenweg, C. Innovative decoupling system for the seismic protection of masonry infill walls in reinforced concrete frames. *Eng. Struct.* **2019**, *197*, 109435. [CrossRef]
39. De Angelis, A.; Pecce, M.R. The role of infill walls in the dynamic behavior and seismic upgrade of a reinforced concrete framed building. *Front. Built Environ.* **2020**, *6*, 590114. [CrossRef]
40. Bikçe, M.; Emsen, E.; Erdem, M.M.; Bayrak, O.F. An investigation on behavior of RC frames with non-interacting infill wall. *Eng. Struct.* **2021**, *245*, 112920. [CrossRef]
41. Mohammadi, M.; Akrami, V.; Mohammadi-Ghazi, R. Methods to improve infilled frame ductility. *J. Struct. Eng.* **2011**, *137*, 646–653. [CrossRef]
42. Vardarli, B. Locked Bricks Without Mortar. Turkish Patent TR200903095U, 21 May 2009.
43. Preti, M.; Bettini, N.; Plizzari, G. Infill walls with sliding joints to limit infill-frame seismic interaction: Large-scale experimental test. *J. Earthq. Eng.* **2012**, *16*, 125–141. [CrossRef]
44. Totoev, Y.; Harthy, A.A. Semi-interlocking masonry as infill wall system for earthquake resistant buildings: A review. *J. Eng. Res.* **2016**, *13*, 33–41. [CrossRef]
45. Palios, X.; Fardis, M.N.; Strepelias, E.; Bousias, S.N. Unbonded brickwork for the protection of infills from seismic damage. *Eng. Struct.* **2017**, *131*, 614–624. [CrossRef]
46. Silva, L.; Vasconcelos, G.; Lourenço, P.; Akhoundi, F. Experimental evaluation of a constructive system for earthquake resisting masonry enclosure walls. In Proceedings of the 16th World Conference on Earthquake Engineering (WCEE), Santiago, Chile, 9–13 January 2017. [CrossRef]
47. Preti, M.; Migliorati, L.; Giuriani, E. Experimental testing of engineered masonry infill walls for post-earthquake structural damage control. *Bull. Earthq. Eng.* **2015**, *13*, 2029–2049. [CrossRef]
48. Morandi, P.; Milanesi, R.R.; Magenes, G. Innovative solution for seismic-resistant masonry infills with sliding joints: In-plane experimental performance. *Eng. Struct.* **2018**, *176*, 719–733. [CrossRef]
49. Milanesi, R.R.; Morandi, P.; Manzini, C.F.; Albanesi, L.; Magenes, G. Out-of-plane response of an innovative masonry infill with sliding joints from shaking table tests. *J. Earthq. Eng.* **2022**, *26*, 1789–1823. [CrossRef]
50. Jin, W.; Zhai, C.; Kong, J.; Liu, W.; Zhang, M. In-plane and out-of-plane quasi-static tests on RC frames with a new type of frame-isolated infills. *Eng. Struct.* **2021**, *246*, 113079. [CrossRef]
51. Chen, Z.; Zhou, Y.; Guo, Y.; Zhong, G.; Shi, F.; Fang, X. Empirical drift-based fragility function and loss estimation for the damped masonry infill wall in the reinforced concrete frame under in-plane cyclic loading. *Eng. Struct.* **2025**, *343*, 120971. [CrossRef]
52. Bolis, V.; Stavridis, A.; Preti, M. Numerical investigation of the in-plane performance of masonry-infilled RC frames with sliding subpanels. *J. Struct. Eng.* **2017**, *143*, 04016168. [CrossRef]
53. Zhang, M.; Ding, J.; Jin, W.; Ding, K.; Ren, M. Study on in-plane/out-of-plane seismic performance of masonry-infilled RC frame with openings and a new type of flexible connection. *Bull. Earthq. Eng.* **2024**, *22*, 2201–2233. [CrossRef]
54. Milijaš, A.; Marinković, M.; Butenweg, C.; Klinkel, S. Experimental investigation on the seismic performance of reinforced concrete frames with decoupled masonry infills: Considering in-plane and out-of-plane load interaction effects. *Bull. Earthq. Eng.* **2024**, *22*, 7489–7546. [CrossRef]
55. Manojlovski, F.; Tubaldi, E.; Sheshov, V.; Rakicevic, Z.; Bogdanovic, A.; Bojadjieva, J.; Shoklarovski, A.; Poposka, A.; Ivanovski, D.; Kitanovski, T.; et al. Flexible joints for seismic-resilient design of masonry-infilled RC frames. *Sci. Data* **2025**, *12*, 1266. [CrossRef] [PubMed]
56. Morandi, P.; Kurukulasuriya, M.; Milanesi, R.R.; Bolognini, D.; Grottoli, L.; Dacarro, F.; Magenes, G. Dynamic shaking table out-of-plane tests on weak masonry infills with and without previous in-plane loading. *J. Build. Eng.* **2025**, *100*, 111670. [CrossRef]

57. Rousakis, T.; Ilki, A.; Kwiecień, A.; Viskovic, A.; Gams, M.; Triller, P.; Ghiassi, B.; Benedetti, A.; Rakicevic, Z.; Colla, C.; et al. Deformable polyurethane joints and fibre grids for resilient seismic performance of reinforced concrete frames with orthoblock brick infills. *Polymers* **2020**, *12*, 2869. [CrossRef] [PubMed]
58. Kouzelis, L.; Moretti, M.L. On the out-of-plane strength of masonry infills encased in RC frames. *Appl. Sci.* **2025**, *15*, 10382. [CrossRef]
59. Asgarkhani, N.; Kazemi, F.; Jankowski, R. Machine-learning based tool for seismic response assessment of steel structures including masonry infill walls and soil-foundation-structure interaction. *Comput. Struct.* **2025**, *317*, 107918. [CrossRef]
60. Furtado, A.; Ramos, T.; Rodrigues, H.; Arêde, A.; Varum, H.; Tavares, P. In-plane response of masonry infill walls: Experimental study using digital image correlation. *Procedia Eng.* **2015**, *114*, 870–876. [CrossRef]
61. Onat, O.; Yön, B. Elimination of a measurement problem: A robust prediction model for missing eigenvector value to assess earthquake-induced out-of-plane failure of infill wall. *Measurement* **2019**, *144*, 88–104. [CrossRef]
62. Guerrero, N.; Martínez, M.; Picón, R.; Marante, M.E.; Hild, F.; Roux, S.; Flórez-López, J. Experimental analysis of masonry infilled frames using digital image correlation. *Mater. Struct.* **2014**, *47*, 873–884. [CrossRef]
63. Mojsilović, N.; Salmanpour, A.H. Masonry walls subjected to in-plane cyclic loading: Application of digital image correlation for deformation field measurement. *Int. J. Mason. Res. Innov.* **2016**, *1*, 165–187. [CrossRef]
64. Chia, W.K. Photogrammetric Determination of Large-Scale Masonry Wall Deformation and Curvature from 3D Displacement Fields. Master's Thesis, National Yang Ming Chiao Tung University, Hsinchu, Taiwan, 2022.
65. Pantoja-Rosero, B.G.; Saloustros, S.; Achanta, R.; Beyer, K. Image-based geometric digital twinning for stone masonry elements. *Autom. Constr.* **2023**, *145*, 104632. [CrossRef]
66. Marendić, A.; Gajski, D.; Duvnjak, I.; Paar, R. Evaluation of photogrammetric methods for displacement measurement during structural load testing. *Remote Sens.* **2025**, *17*, 2569. [CrossRef]
67. de Moraes, F.R.; da Silva, I. Assessment of submillimeter precision via structure from motion technique in close-range capture environments. *arXiv* **2024**, arXiv:2409.15602. [CrossRef]
68. *TS 11758-1*; Polymer Bituminous Sheets for Waterproofing—Used by Torch Welding—Part 1: Specifications. Turkish Standards Institution (TSE): Ankara, Türkiye, 2002.
69. *EN 13163:2012+A2:2016*; Thermal Insulation Products for Buildings—Factory-Made Expanded Polystyrene (EPS) Products—Specification. European Committee for Standardization (CEN): Brussels, Belgium, 2016.
70. *EN 1504-3:2005*; Products and Systems for the Protection and Repair of Concrete Structures—Definitions, Requirements, Quality Control and Evaluation of Conformity—Part 3: Structural and Non-Structural Repair. European Committee for Standardization (CEN): Brussels, Belgium, 2005.
71. *ACI 374.2R-13*; Guide for Testing Reinforced Concrete Structural Elements Under Slowly Applied Simulated Seismic Loads. American Concrete Institute: Farmington Hills, MI, USA, 2013.
72. Agisoft LLC. *Agisoft Metashape*, Version 1.6.2; Computer Software; Agisoft LLC: St. Petersburg, Russia, 2020. Available online: https://www.agisoft.com/ (accessed on 31 May 2026).

Disclaimer/Publisher's Note: The statements, opinions and data contained in all publications are solely those of the individual author(s) and contributor(s) and not of MDPI and/or the editor(s). MDPI and/or the editor(s) disclaim responsibility for any injury to people or property resulting from any ideas, methods, instructions or products referred to in the content.